Body mechanics, optimality, and sensory feedback in the human control of complex objects

Reza Sharif Razavian[1,2†*], Mohsen Sadeghi[1,2†], Salah Bazzi[2,3†], Rashida Nayeem[2], Dagmar Sternad[1,2,3,4]

1 Department of Biology, Northeastern University, Boston, MA, USA

2 Department of Electrical and Computer Engineering, Northeastern University, Boston, MA, USA

3 Institute for Experiential Robotics, Northeastern University, Boston, MA, USA

4 Department of Physics, Northeastern University, Boston, MA, USA

† These authors contributed equally

* razavian.reza@nau.edu

1 Abstract

Humans are adept at a wide variety of motor skills including the handling of complex objects and using tools. Advances to understand the control of voluntary goal-directed movements have focused on simple behaviors such as reaching, uncoupled to any additional object dynamics. Under these simplified conditions, basic elements of motor control, such as the roles of body mechanics, objective functions, and sensory feedback, have been studied in isolation, and the interactions between

these element have received less attention. This study examined a task with internal dynamics, inspired by the daily skill of transporting a 'cup of coffee', with additional expected or unexpected perturbations to probe the structure of the controller. Using optimal feedback control (OFC) as basis, it proved necessary to endow the model of the body with mechanical impedance to generate the kinematic features observed in the human experimental data. The addition of mechanical impedance revealed that simulated movements were no longer sensitively dependent on the objective function, a highly debated cornerstone of optimal control. Further, feed-forward replay of the control inputs was as successful in coping with perturbations as when feedback, or sensory information, was included. These findings suggest that when the motor control model incorporates a representation of the mechanical properties of the limb, i.e., embodies its dynamics, the specific objective function and sensory feedback become less critical and complex interactions with dynamic objects can be successfully managed.

Introduction

Humans show remarkable dexterity in a wide range of skills, from juggling balls to a host of seemingly mundane actions in everyday life. For example, reaching for a glass of wine, swirling it, and leading it to one's mouth to drink involves interacting with—and controlling—the complex fluid dynamics acting upon the hand. Handling such complex and potentially even chaotic dynamics is a feat that modern robots have failed to accomplish so far. Also in human motor neuroscience, most research on human movement control to date have only addressed relatively simple movements, such as moving one's hand from point to point, void of any

dynamics arising from objects and interactions with the environment. Consequently, models of human motor control may have remained relatively simple as they did not have to deal with complex and sometimes unpredictable interaction dynamics. Human manipulation of objects—the essence of tool use—has remained largely beyond neuroscientists' reach. To better understand how the brain controls and coordinates movements, we must look beyond unconstrained reaching movements and study richer and more naturalistic behaviors that reveal the underlying control principles.

Characterization of a dynamical system and its control requires exciting inputs that perturb the dynamical modes [1, 2]. Hence, the application of external perturbations has been the widely used method to interrogate the human motor system [3–5]. Beyond controlled external perturbations, another way to excite the motor system and reveal its dynamical modes is to expose the motor system to interactions with the world as are naturally inherent in daily activities. For example, previous studies examined more naturalistic tasks playing pool billiards [6, 7], bouncing a ball on a paddle [8], or interacting with dynamically complex objects, such as carrying a cup of coffee [9, 10] or striking a target with a whip [11, 12]. The study of such naturalistic interactions suggested that most of the conventional control objectives, such as maximizing smoothness [13], or minimizing effort [14], are not sufficient to account for human behavior. When investigating a task such as transporting a cup of coffee, more nuanced and object-centric objectives seem to be in play that are concerned with stability and predictability of the interactions [15, 16], and with minimizing the transient behavior of object that is being controlled [14]. Expanding on these insights, this study aims to understand complex interactions, with a focus on how embodiment affects higher-level control

objectives, as well as the role of sensory feedback in the control process.

In interactions with the external world, physical properties of the body, especially the mechanical impedance of the limbs, has been identified as critical [17, 18]. Due to its ability to store and dissipate mechanical energy, impedance affords stability in the presence of sensorimotor delays [19] or when facing perturbations [5]. Impedance has been proposed as a dynamic primitive that interfaces the body with the external world and shapes basic patterns of movements [20, 21]. The controller determines the *zero-force trajectories* in interactions with the environment, and the observable movements arise as a consequence of this interaction. From a physiological perspective, the central nervous system sets virtual or equilibrium-point trajectories via tuning of the phasic and tonic stretch reflexes [22–24]. However, to create rich behavior, the computational principles that generate more complex reference trajectories have remained elusive. This work sought to uncover how the inherent mechanics of the body—the 'embodied intelligence'—and the characteristics of the neural controller influence one another in both the choice of control objectives and the use of sensory feedback.

In computational motor neuroscience, several lines of research have pursued the framework of optimal control as a model for the human motor controller [25]. The fundamental assumption in the optimal control framework is that the brain selects movements to optimize a certain *objective* or *cost function*. The nature of this objective function has been the focus of many studies and several candidates have been proposed that are either based on kinematics [26–31], kinetics [32, 33], or energetics [34, 35]. All of these objectives described human movements well in their respective experimental contexts. However, these costs are not completely independent and free to choose by the brain. Wong and colleagues [35] showed that

kinematic smoothness arose as a by-product of physiological energy minimization, without any explicit kinematics-related cost function. This finding suggests that including more bio-fidelic features in the control model may achieve desired features in human behavior in a less top-down dictated fashion. In this vein, mechanical impedance of the body, with its ability to store and dissipate energy, plays a critical role in defining the energetic landscape of the movements. Therefore, it is expected that the energy buffering of impedance affects properties of the controller, specifically the objective function.

The neural controller possesses feedback and feed-forward control pathways that have been recognized as early as 1899 [36]. However, the exact interplay between feed-forward and feedback control mechanisms and their dependency on different task scenarios is still under debate [37, 38]. While an essential element for many accuracy-requiring task, for rapidly evolving physical interactions, such as carrying a cup filled with sloshing coffee, the sensorimotor information transmission is too slow to ensure successful feedback-based corrections. A more likely mechanism for instantaneous interaction dynamics is mechanical impedance as it affords rapid corrective responses without relying on neural signal transmission [19, 39]. Indeed, previous results on interaction with the cup-and-ball system already highlighted that simple feed-forward models that included impedance reproduced behavior well [10, 14]. However, it remains unclear how feedback and feed-forward processes interact with mechanical impedance in situations that require unplanned and rapid, yet complex responses. This study will apply expected and unexpected perturbations to examine the interplay of feed-forward and feedback processes in interaction with impedance.

In overview, this study used the dynamically complex experimental task of

transporting a simplified 'cup of coffee' to examine how interfacing the controller with the body's mechanical impedance affects the resulting behavior. To generate rich and informative data, the experiment included predictable and unpredictable perturbations in addition to the complex interaction forces generated through the object's internal dynamics. The optimal feedback control (OFC) framework was used as the model for the neural controller [40]. Simulations scrutinized how inclusion of impedance in the model changed its behavior under different objective functions and involvement of sensory feedback. We hypothesized that mechanical impedance was a critical component to accurately generate interactions with the complex object (Hypothesis 1), that the specifics of the objective function become less prominent due to the energy buffering of impedance (Hypothesis 2), and that, for the same reasons, sensory feedback plays a subordinate role in this dynamically rich behavior (Hypothesis 3).

2 Methods

2.1 Experiments

2.1.1 Participants

Eleven healthy right-handed individuals participated in the experiment (19-25 years old, 8 females). None of the participants had any history of neurological disorders or biomechanical injuries in their upper limbs. Each subject provided written consent to the experimental procedures prior to participation. All subjects were given monetary compensation for their participation. The study was approved by the Institutional Review Board of Northeastern University.

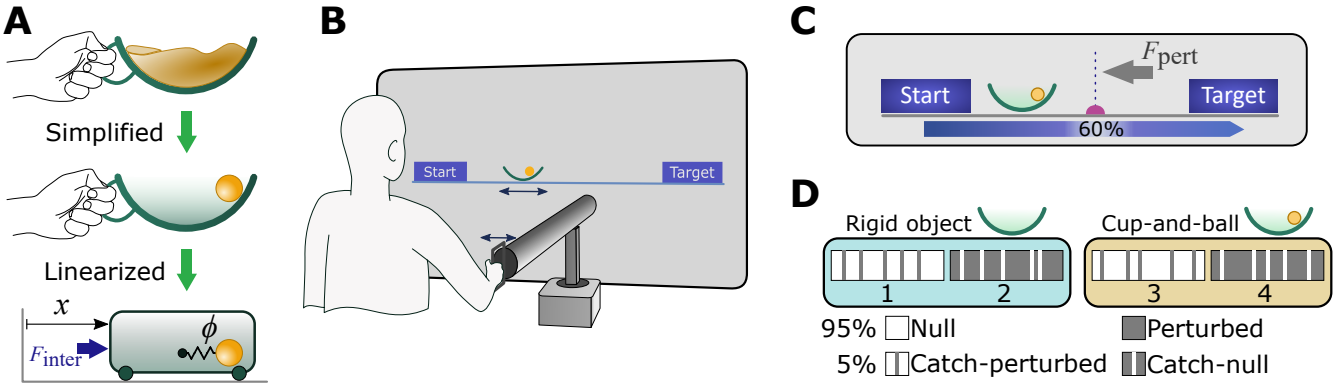

Fig 1. Experimental apparatus and task design. **A**. Inspired by the daily activity of carrying a cup of coffee, the simplified model of a cup with a ball inside mimicked the internal dynamics of this complex object. The dynamics of this simplified cup-and-ball system was generated by the linearizing the equations of motion of an equivalent cart-and-pendulum system, where the cart was directly driven by the interaction force, F_{inter}, applied by the hand to the cart. **B**. The linearized cup-and-ball system was implemented in a virtual environment although still displayed as a 2D semicircular cup with a ball (bob of the pendulum) sliding inside. Participants could directly control the displayed cup via a robotic manipulandum; they received online haptic feedback about the dynamics of the system. The task involved moving the cup on a horizontal line from the start to the target box (32.5 cm distance) without losing the ball. **C**. To enhance the control demands, a perturbation was applied to the cup at 60% of the total path length. The perturbation was an impulse-like force of 20 ms duration and 20 N magnitude, applied in the opposite direction of the cup movement. The location of the perturbation was visually displayed as a 'speed bump', but did not propel the cup in the vertical direction. **D**. Experimental design: Four experimental conditions were tested in 4 blocks, each with 100 trials: in Blocks 1 and 2 subjects interacted with the rigid object (ball fixed to the cup); in Blocks 3 and 4 the full dynamics of the cup-and-ball system was presented. Blocks 1 and 3 contained 95% unperturbed 'null' trials and 5% randomly interspersed perturbation trials, acting as *catch* trials. Blocks 2 and 4 presented 95% perturbation trials, with 5% unperturbed trials as random *catch* trials. All catch trials were visually indistinguishable from the rest of the trials in the same block.

2.1.2 Moving a Complex Object—a Cup with a Ball Rolling Inside

The experimental task was inspired by the daily activity of carrying a cup of coffee. Unlike transporting a rigid object, carrying an object with internal degrees of freedom creates nonlinear and potentially even chaotic interaction forces onto the hand [9, 16, 41, 42]. To examine such interactions, in previous work we simplified

the 'cup of coffee' to a 2D semi-circular cup with a ball sliding inside and moving on a horizontal line. Despite its simplicity, this model maintained the key elements of underactuation, while providing mathematical tractability and virtual implementation of the task (**Fig. 1A**). This original cup-and-ball system was equivalent to a 2D cart-and-pendulum system, where the bob of the suspended pendulum corresponded to the ball, and the 2D arc of the cup was the circular path of the pendular bob.

This study employed optimal feedback control (OFC [43], see section 2.2.1) as a framework for the controller to explore the contributions of impedance, optimality criteria, and sensory feedback. As this OFC was developed for linear systems, the equations of motion of the cup-and-ball system were linearized around the ball's rest position at the bottom of the cup. This linearization led to the following equations of motion:

$$(M+m)\ddot{x} = -ml\ddot{\phi} + F_{inter} + F_{pert} \tag{1}$$

$$l\ddot{\phi} = -g\phi - G\ddot{x}. \tag{2}$$

where x and ϕ are the cup position and ball angle, respectively. F_{inter} is the force of the hand interacting with the cup, and F_{pert} is an external perturbation force. The system parameters $M = 3$ kg and $m = 0.3$ kg are the cup and ball masses, respectively. The pendulum length $l = 0.5$ m corresponds to the radius of the cup; $g = 9.81$ m/s^2 is the gravitational acceleration. $G = 5$ is the coupling term between the cup and the ball dynamics. Since the physical limitations of the robot did not allow simulating arbitrary object parameters, the value of G was set to be

greater than 1 to make the ball more agile and responsive to cup accelerations, while satisfying the constraints of the robot.

This linearized model was used both in the virtual implementation for the human experiments, as well as in the simulations of different control models. While the linearized model no longer exhibited chaotic behavior, it still presented considerable challenges due to the underactuated degrees of freedom. A previous study demonstrated that the linearized version of the cup-and-ball system demanded slightly higher interaction forces as well as contained a more prohibitive anti-resonance frequency, while other control challenges were similar to the nonlinear system [44]. Hence, the linearization was not expected to affect the purpose of this study.

Despite linearization, the virtual environment displayed the cup and ball as in previous studies; the angle of the ball in the cup corresponded to the linear state ϕ in (2). As a control condition for the cup-and-ball system, the internal degree of freedom of the system, i.e., the ball, was constrained by fixing it to the bottom of the cup. This rigid-object condition essentially reduced the behavior to an unconstrained reaching movement with an increased hand mass. The inertia of this rigid object was matched to equate the sum of the cup and ball masses in the non-rigid system. The rigid object was displayed as an empty cup for visual consistency, however its inertia matched the total mass of the cup and ball.

2.1.3 Experimental Apparatus

For both object types—rigid object and cup-and-ball—the dynamics was simulated and rendered in a virtual environment, where participants interacted with the object via a haptic robotic manipulandum (HapticMaster, FCS Control Systems, The Netherlands [45]). Subjects received haptic feedback about the object dynamics

and interaction forces via the robotic handle (**Fig. 1B**). The robot was admittance controlled: the measured interaction force applied by the subjects on the robot handle determined its acceleration by rearranging the cup's equation of motion (1) as:

$$a_{robot} = \frac{1}{M+m}\left(F_{inter} + F_{ball} + F_{pert}\right) \tag{3}$$

with $F_{ball} = -ml\ddot{\phi}$. The desired acceleration of the robot in (3) was enforced by its internal controller running at 4 kHz. F_{ball} was updated at a median sampling rate of 641 Hz (interquartile range 500-709 Hz) using the actual acceleration of the robot and the ball's equation of motion (2). The measured interaction force as well as the kinematics of the movements were read out from the robot at the same rate of 641 Hz.

The visual information about the object movement and the virtual environment, i.e., the target boxes and the added perturbation bump, were displayed on a vertical projection screen with a frame rate of 60Hz. The total latency of the robotic interface and the visual projection, defined as the time difference between the moment the robot's handle moves until the time the movement is displayed on the screen, was 33 ms$\pm$17 ms. To measure this latency, a single video camera was used to simultaneously capture the robot's handle and the displayed cup position. This video was processed offline to digitize the positions of the robot and the cup, and the time lag between the two position signals were calculated via cross-correlation.

2.1.4 Experimental Design and Procedure

Participants stood in front of the projection screen and grasped the handle of the robotic manipulandum, by which they could control the displayed object on the screen (**Fig. 1B**). They were instructed to move the object via the robot's handle along a horizontal line from a starting box (left) to a target box (right) displayed on the screen. The physical distance between the centers of start and target box was 32.5 cm. Each cup-and-ball trial started with the ball resting at the bottom of the cup. If the ball angle surpassed the rim of the cup during the movement, i.e., $\phi > \pm 45°$, the ball would 'escape', and the trial would be terminated as a failed attempt. The failed trials were not repeated. A successful trial ended when the cup was fully inside the target box and its speed fell below 5 mm/s. To avoid lengthy adjustments to home in to the target, the start and target boxes were 30% wider than the width of the cup, allowing ±5.3 mm tolerance. For the rigid-object condition, there were no failures and all trials were considered successful.

To promote consistency across subjects, participants were instructed via feedback to finish each trial within 1.4 s (±20%) for the rigid object, and 1.8 s (±20%) for the cup-and-ball system. These movement times were chosen from preferred durations measured in pilot experiments. The movement durations were displayed at the end of each trial with the text color indicating whether the duration was within the acceptable bound (green), too fast (yellow), or too slow (red). This feedback was merely informative and violation of the desired movement time did not lead to any explicit penalties, nor exclusion of the trial from analysis. Overall, subjects very quickly learned and adhered to the suggested movement time (see Behavioral Results).

In many trials, an external perturbation was applied that disturbed the move-

ments (**Fig. 1C**). The perturbation was an impulsive force of magnitude $F_{pert} =$ 20N, applied to the cup for 20 ms in the opposite direction of the movement, without any effect in the vertical direction. This perturbation was applied at a fixed location 60% into the movement distance towards the target. With the exception of the *catch* trials (see below), the existence of the perturbation in a trial was cued using a visual 'speed bump' (**Fig. 1C**). Therefore, the participants were aware of its presence or absence before the trial began.

Each participant performed the task both with the rigid object and with the cup-and-ball system in a total of 4 blocks of 100 trials each (**Fig. 1D**). The first two blocks involved performing the task with the rigid object, blocks 3 and 4 presented the cup-and-ball system. Block 1 consisted of 95% unperturbed ('null') trials and 5% perturbation trials ('catch-perturbed'), randomly interspersed across the block. Subjects were unaware of the perturbation prior to the trial onset and there was no visual cue signaling the perturbation. Block 2 consisted of 95% perturbed trials (speed bump shown) and 5% null trials ('catch-null'), randomly interspersed across the block. Unlike the 'catch-perturbed' trials in Block 1, the 'catch-null' trials in Block 2 were also cued with a visually displayed 'speed-bump' on the way to the target like the remaining 95% of the trials in that block. Hence, subjects expected a perturbation, but no force was applied. Blocks 3 and 4 were the same as Blocks 1 and 2, respectively, except that subjects interacted with the cup-and-ball system. The order of the blocks was the same for all participants. Overall, each participant performed 400 trials. Each block lasted approximately 10-12 minutes, with sufficient break time given between the blocks. The experiment lasted approximately 1 hour from beginning to end.

2.1.5 Dependent Measures and Statistical Analysis of the Experimental Data

A first analysis aimed to assess whether there were any improvements during each of the four blocks. This was particularly relevant in the cup-and-ball condition that posed more coordination challenges. Using movement time as an indicator, it was determined as follows: trial onset was defined as the time when the cup velocity exceeded 5 mm/s in direction of the target; the trial ended when the cup was fully inside the target box and its speed fell below 5 mm/s. To evaluate whether movement time changed over the course of practice, a Wilcoxon signed-rank test (within-subject, N=11) compared the median trial duration of the first 25 and last 25 trials of each block. This non-parametric test was appropriate as the distributions of this variable did not meet the normality criterion.

To evaluate how subjects coped with the expected perturbations in the perturbed trials, the interaction forces were examined. Inspection of the trials in both the rigid-object and cup-and-ball trials showed that the force exhibited a characteristic discontinuity immediately following the perturbations (see results). To quantify this observed phenomenon in the different conditions, the force value at the onset of the perturbation was compared against its value immediately after the 20 ms interval of the perturbation. For each participant, the difference values of $F_{pre} - F_{post}$ were tested against zero using unpaired t-tests. These tests were conducted separately for the rigid-object and the cup-and-ball conditions.

The cup velocity in the cup-and-ball condition rebounded after the perturbation. In the data, this rebound started immediately after the end of the perturbation. To quantify this feature, the cup's peak acceleration following the perturbation was identified in each trial. The peak values and the time of the peak to the end

of the perturbation were analyzed.

2.2 Control Models

To identify the necessary elements in a control model for this task, several models were developed and compared with the experimental behavior. All models were based on the optimal feedback control framework as presented in [43]. To simulate the experimental data, the control models needed to successfully transport the cup-and-ball to the target without losing the ball. Two basic control models were developed (**Fig. 2**): The first model included the dynamics of the object, cup-and-ball and also the rigid object, together with a simplified inertial and muscular dynamics of the arm (**Fig. 2A**, section 2.2.2). This basic OFC model was contrasted against a second model that further included a simplified mechanical impedance element (**Fig. 2B**, section 2.2.3). This constant impedance stood as proxy for the compliant dynamics of the arm. These two models served as the basis to study the interplay between impedance, cost functions, and corrections via sensory feedback.

The starting hypothesis was that arm impedance critically affected the model behavior, especially when additional external perturbations occurred. The two basic model structures compared the simulated behavior with both the rigid and the cup-and-ball object. These models included the most frequently used cost function that minimized effort [32]. The second point of interest was the effect of the cost function on behavior, once impedance was included. To address this question, the two OFC models compared the behavior using the cost functions minimum-effort with minimum-jerk (**Fig. 2C, D**, sections 2.2.4 and 2.2.5). The third analysis evaluated the role of sensory feedback, especially when facing unexpected external

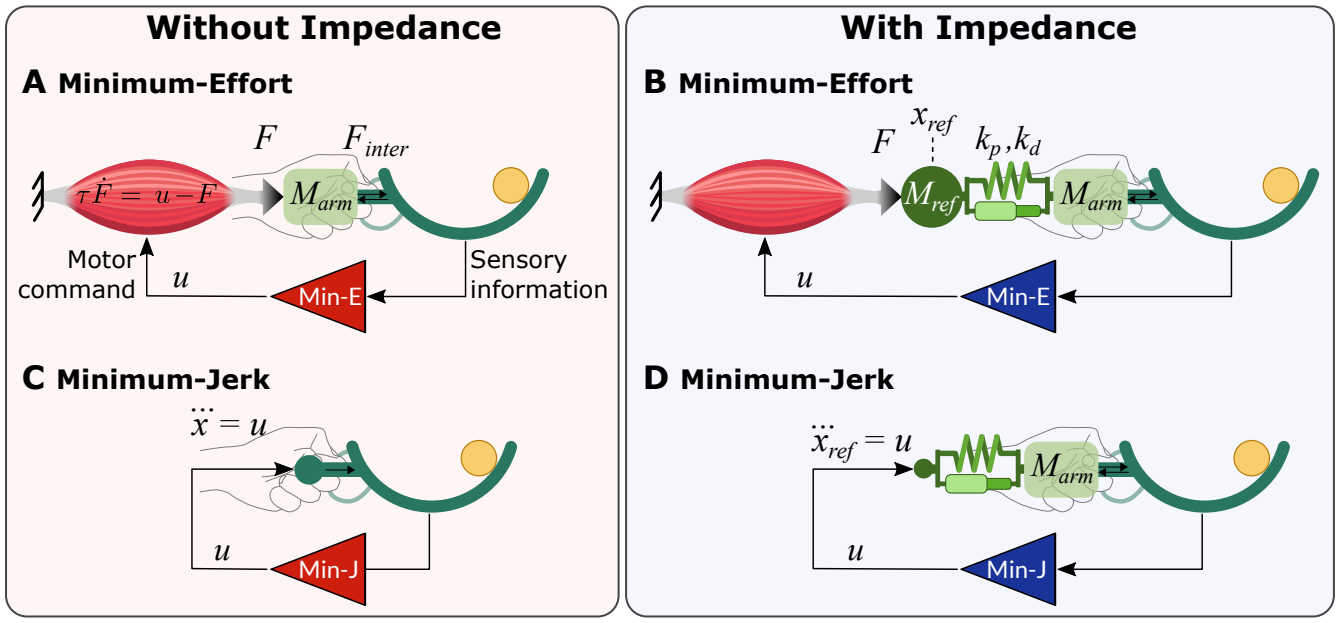

Fig 2. A. The basic OFC model included a simplified muscle model. This muscle muscle model produced force F according to the motor command u; minimizing u was a proxy for minimizing neuromuscular effort. The interaction force was measured at the interface between the hand mass M_{arm} and the object. **B.** The second model included an impedance element (stiffness and damping k_p, k_d) and an inertia, M_{ref}, that was placed between the muscle model and the hand/object. The inertial dynamics of M_{ref} produced the reference trajectory x_{ref} under the applied forces. **C.** The minimum-jerk variant of the OFC model did not include a muscle model; instead, the controller outputted the jerk of the cup trajectory. Thus, minimizing u results in a minimum-jerk trajectory that took into account the dynamics of the object. **D.** With impedance in the model, the minimum-jerk variant of the OFC model prescribed the kinematics of the reference trajectory for the impedance elements.

perturbations. This analysis focused on the *catch trials* and compared the basic feedback control model with a variant that eliminated feedback.

2.2.1 Basics of Stochastic Optimal Feedback Control

The optimal feedback control (OFC) model that had been frequently used in movement neuroscience represented the neural controller as a linear quadratic Gaussian controller that dealt with additive and multiplicative sensory and motor noise [43].

This optimal controller determined the control command u that minimized the quadratic cost function:

$$J = \sum_{t=0}^{N-1} \left(\mathbf{x}_t^T \mathbf{Q}_t \mathbf{x}_t + u_t^T R_t u_t \right) + \mathbf{x}_N^T \mathbf{Q}_N \mathbf{x}_N, \tag{4}$$

subject to:

$$\begin{aligned} \text{Dynamics:} \quad & \mathbf{x}_{t+1} = \mathbf{A}\mathbf{x}_t + \mathbf{B}\left(\mathbf{I} + \boldsymbol{\varepsilon}_t\right) u_t + \boldsymbol{\xi}_t, \\ \text{Sensory feedback:} \quad & \mathbf{y}_t = \mathbf{H}\left(\mathbf{I} + \boldsymbol{\epsilon}_t\right) \mathbf{x}_t + \boldsymbol{\omega}_t \end{aligned} \tag{5}$$

where $\mathbf{x}$ is the state vector, and $\boldsymbol{\xi}$ and $\boldsymbol{\varepsilon}$ represent additive and multiplicative (control-dependent) motor noise terms, respectively. The subscript t represents the time-step, and N is the total number of time steps in the simulations. The terms R_t and $\mathbf{Q}_t$ in the objective function (4) are weights for effort and accuracy costs, respectively. For all simulations, we used $R_t = 1$ for all t. $\mathbf{Q}_t$ was separately defined for each model, depending on the number of states in that model (see below). The sensory feedback ($\mathbf{y}_t$) contained additive ($\boldsymbol{\omega}$) and multiplicative (state-dependent; $\boldsymbol{\epsilon}$) sensory noise. The optimal control law was then calculated as a feedback gain $u_t = \mathbf{L}^* \hat{\mathbf{x}}$, where the estimated state vector $\hat{\mathbf{x}}$ was calculated based on the delayed feedback signal and the system dynamics (refer to [43] for details on the implementation of sensory delay and the calculation of feedback gains). For our simulations, the sensory delay was set to 50 ms. The motor noise terms $\boldsymbol{\xi}$ and $\boldsymbol{\varepsilon}$ were zero mean Gaussian noise with the standard deviations of 10^{-4} and 1, respectively (with appropriate SI units). The covariance matrix for the additive sensory noise was a diagonal matrix defined as $\boldsymbol{\omega} = diag(10^{-5})$, and

Table 1. List of model parameters that were kept the same in all models.

Parameter	Description	Value*
d	Sensory delay	0.05
ε	Standard deviation of control-dependent process noise	1
ϵ	Standard deviation of state-dependent sensory noise	0
ξ	Standard deviation of additive process noise†	1×10^{-4}
$\boldsymbol{\omega}$	Covariance matrix of additive sensory noise	Diag(1×10^{-5})
$\boldsymbol{\eta}$	Covariance matrix of internal noise in state estimator [43]	Diag(1×10^{-8})
n	Number of time-steps to hold the object at target	50
τ	Time constant of the first-order muscle dynamics	0.03

* In corresponding SI units and appropriate dimensions.
† Only for control-affected state (e.g., muscle force) and the perturbation state.

no state dependency was considered for the sensory noise ($\boldsymbol{\epsilon} = 0$; see **Table 1** for a full description of the parameter values). The following sections present each model variant with its state vector and dynamic properties (matrices **A**, **B** and **H** in equations 5).

2.2.2 Minimum Effort Model Without Impedance.

The conventional OFC model is often formulated to minimize the square of neuromuscular effort [32, 46]. To include a proxy for neuromuscular dynamics in this model, the equations of motion of the object (1) were coupled with a first-order muscle model [47] as shown in **Fig. 2A**:

$$\begin{aligned} (M_{arm} + M + m)\ddot{x} &= -ml\ddot{\phi} + F + F_{pert} \\ l\ddot{\phi} &= -g\phi - G\ddot{x}. \\ \tau\dot{F} &= u - F \end{aligned} \tag{6}$$

where F is the muscle output force applied to the hand (M_{arm}) and indirectly

to the cup-and-ball (**Fig. 2A**). Note that the interaction force F_{inter} in equation 1 was not the same as the muscle output force F, as the latter needed to be calculated between the hand and the cup-and-ball system. To be consistent with the experimentally measured values, the interaction force was calculated from (1) given the simulated x and ϕ trajectories.

The perturbation force F_{pert} was an impulse force that acted on the cup-and-ball system for a short time (20 ms) at the time the cup traveled 60% of the target distance. For null trials, $F_{pert} = 0$ at all times. The numeric values of system parameters in the simulations were: $M = 3$ kg, $m = 0.3$ kg $l = 0.5$ m, $g = 9.81$ m/s^2, $G = 5$, and $\tau = 30$ ms. The hand mass (M_{arm}) was a free parameter in the model fitting procedures (see section 2.3).

Given the equations of motion, the model could be written in the standard state-space form as follows:

$$
\begin{aligned}
\mathbf{x} &= \left[x,\ \phi,\ \dot{x},\ \dot{\phi}, F,\ F_{pert}\right]^T \\
\mathbf{A} &= \begin{bmatrix}
0 & 0 & 1 & 0 & 0 & 0 \\
0 & 0 & 0 & 1 & 0 & 0 \\
0 & \frac{mg}{\alpha} & 0 & 0 & 1/\alpha & 1/\alpha \\
0 & \frac{-g}{l}(1+\frac{Gm}{\alpha}) & 0 & 0 & \frac{-G}{l\alpha} & \frac{-G}{l\alpha} \\
0 & 0 & 0 & 0 & -1/\tau & 0 \\
0 & 0 & 0 & 0 & 0 & 0
\end{bmatrix} \\
\mathbf{B} &= [0,\ 0,\ 0,\ 0,\ 1/\tau,\ 0]^T \\
\mathbf{H} &= \mathbf{I}_{6\times 6}.
\end{aligned}
\tag{7}
$$

where $\alpha = m + (M + M_{arm}) - mG$.

In Blocks 2 and 4, participants anticipated the impulsive perturbation. This anticipation also had to be modeled within the OFC framework. Note that the optimal controller's behavior is only influenced by the state-space matrices $\mathbf{A}$, $\mathbf{B}$, and $\mathbf{H}$, as well as $\mathbf{Q}$. Therefore, the perturbation needed to be included as a state to embed such information in matrix $\mathbf{A}$. Further note that the position-dependent perturbation, as in the experiments, could not be modeled in a linear state-space form; instead, the perturbation was implemented as time-dependent, and its timing was manually adjusted so that the perturbation occurred at the right position in the simulations. To implement this perturbation, the zero-dynamic state variable F_{pert} was set to -20 N, but its corresponding terms $\mathbf{A}_{3,6}$ and $\mathbf{A}_{4,6}$ were zero when the perturbation force was inactive. These state-space equations were subsequently time-discretized using Euler integration with time-step δt =10 ms to be used in the discrete-time optimal control problem of (4), (5). Following time-discretization, the time-dependent matrix $\mathbf{Q}_t$ was defined as:

$$\mathbf{Q}_t = \begin{cases} \text{Diag}\left([p_x,\ p_b,\ p_{\dot{x}},\ 0,\ 0,\ 0]\right) & N - 50 < t \leq N \\ \text{Diag}\left([0, p_b,\ 0,\ 0,\ 0,\ 0]\right) & t \leq N - 50 \end{cases}, \tag{8}$$

with N denoting the total number of time steps. Note that the cost term ($\mathbf{Q}_t$) penalized the cup position (x) and cup velocity ($\dot{x}$) in the last 50 time steps (= 500 ms) of the movement to assure that the object came to rest at the target. The parameters p_x and $p_{\dot{x}}$ in the $\mathbf{Q}_t$ matrix were the penalty values assigned to the cup position and velocity ($p_x = p_{\dot{x}}$ in the simulations). Further, to prevent the ball from escaping during the simulations, the penalty for the ball angle p_b held for the entire movement duration. These free penalty parameters were

obtained by fitting the models to the experimental data. The initial conditions were $x_0 = [-32.5cm, 0, 0, 0, 0, -20N]^T$ and the total simulation time was set to the average participant's trial duration, plus 500 ms hold time.

2.2.3 Minimum Effort Model With Impedance

In human motor control, mechanical impedance of the body has often been approximated by linear spring and damper elements. **Fig. 2B** illustrates how the model of the arm was extended by an impedance. By adding a linear spring k_p and damper k_d to the system, the equations of motion took the form:

$$\begin{aligned}
(M_{arm} + M + m)\ddot{x} &= -ml\ddot{\phi} + k_p(x_{ref} - x) + k_d(\dot{x}_{ref} - \dot{x}) + F_{pert} \\
l\ddot{\phi} &= -g\phi - G\ddot{x} \\
\tau\dot{F} &= u - F \\
M_{ref}\ddot{x}_{ref} &= k_p(x - x_{ref}) + k_d(\dot{x} - \dot{x}_{ref}) + F,
\end{aligned} \tag{9}$$

where x_{ref} represents the reference trajectory for the spring and damper system, i.e., the point the muscle force F is applied (**Fig. 2**B). Note that the muscle force in this case could only indirectly affect the cup-and-ball dynamics via the impedance operator. The non-zero mass M_{ref} in the equations was needed to avoid a mathematical singularity (division by zero) when modeling the system. This point mass can be considered as a lumped-parameter effective mass of the engaged musculature. In this model, the parameters M_{arm}, M_{ref}, k_p and k_d were free parameters found during the model fitting procedure. The standard state-space representation of the model was:

$$\mathbf{x} = \left[x,\ \phi,\ \dot{x},\ \dot{\phi}, F,\ x_{ref},\ \dot{x}_{ref},\ F_{pert}\right]^T$$

$$\mathbf{A} = \begin{bmatrix} 0 & 0 & 1 & 0 & 0 & 0 & 0 & 0 \\ 0 & 0 & 0 & 1 & 0 & 0 & 0 & 0 \\ \frac{-k_p}{\alpha} & \frac{mg}{\alpha} & \frac{-k_d}{\alpha} & 0 & 0 & \frac{k_p}{\alpha} & \frac{k_d}{\alpha} & \frac{1}{\alpha} \\ \frac{k_p G}{l\alpha} & \frac{-g}{l}(1+\frac{Gm}{\alpha}) & \frac{k_d G}{l\alpha} & 0 & 0 & \frac{-k_p G}{l\alpha} & \frac{-k_d G}{l\alpha} & \frac{-G}{l\alpha} \\ 0 & 0 & 0 & 0 & -1/\tau & 0 & 0 & 0 \\ 0 & 0 & 0 & 0 & 0 & 0 & 1 & 0 \\ \frac{k_p}{M_{ref}} & 0 & \frac{k_d}{M_{ref}} & 0 & 1 & \frac{-k_p}{M_{ref}} & \frac{-k_d}{M_{ref}} & 0 \\ 0 & 0 & 0 & 0 & 0 & 0 & 0 & 0 \end{bmatrix} \tag{10}$$

$$\mathbf{B} = [0,\ 0,\ 0,\ 0,\ 1/\tau,\ 0,\ 0,\ 0]^T$$

$$\mathbf{H} = \mathbf{I}_{8\times 8}.$$

The cost term $\mathbf{Q}_t$ was defined as a 8×8 diagonal matrix, with penalty terms considered for the cup position and velocity, and the ball angle, as shown in (8).

2.2.4 Minimum Jerk Model Without Impedance

To study the effects of the objective function in our task, the objective of minimizing effort was contrasted with the objective of maximizing kinematic smoothness. Kinematic smoothness, frequently quantified by the time-derivative of acceleration (jerk), is another widely-discussed objective function for human movements [26, 27, 29, 48]. It must be noted that forces from the ball made the cup trajectory deviate from a pure minimum-jerk profile, i.e., it no longer exhibited a bell-shaped maximally smooth velocity profile [49]. However, the OFC framework could include

other cost terms, such as a penalty on the movement of the ball, to minimize jerk while taking into account the dynamics of the task.

To minimize cup jerk in the model, the equations of motion had to be rewritten to have the cup jerk either as an input or a state. This modification was required to use the quadratic cost function (4)) to minimize the squared value of jerk. In this model, the optimal feedback controller specified the third derivative of the cup position as the control input ($\frac{d}{dt}(\ddot{x}) = u$; **Fig. 2C**). To incorporate this equation into the state-space model, the cup acceleration $\ddot{x}$ was included as an additional state. Note that u directly prescribed the cup kinematics, i.e., the cup movement was forced. Therefore, the muscle model no longer had an effect on the overall system dynamics and was removed. Following this modification, the equations of motion became:

$$\begin{aligned} \dddot{x} &= u \\ l\ddot{\phi} &= -g\phi - G\ddot{x} \end{aligned} \tag{11}$$

Further, because the cup kinematic was fully prescribed by the controller, the perturbation force F_{pert} did not affect the cup movement and was removed from the equations. Therefore, the state-space representation of the dynamics became:

$$
\begin{aligned}
\mathbf{x} &= \left[x,\ \phi,\ \dot{x},\ \dot{\phi},\ \ddot{x}\right]^T \\
\mathbf{A} &= \begin{bmatrix} 0 & 0 & 1 & 0 & 0 \\ 0 & 0 & 0 & 1 & 0 \\ 0 & 0 & 0 & 0 & 1 \\ 0 & \frac{-g}{l} & 0 & 0 & \frac{-G}{l} \\ 0 & 0 & 0 & 0 & 0 \end{bmatrix} \\
\mathbf{B} &= [0,\ 0,\ 0,\ 0,\ 1]^T \\
\mathbf{H} &= \mathbf{I}_{5\times 5}.
\end{aligned}
\tag{12}
$$

As the control commands u in this OFC variant was directly defined as the jerk of cup movement, the penalty term $u_t^T R_t u_t$ in the cost function (4) led to a minimum jerk trajectory, while taking into account the dynamics of the ball and the requirements of the task. For this model, the $\mathbf{Q}_t$ matrix was defined as a 5×5 diagonal matrix with the same ball and cup penalty terms as in (8).

2.2.5 Minimum Jerk Model With Impedance

For the minimum-jerk variant of the model that includes impedance (**Fig. 2D**), the third derivative of the reference trajectory was prescribed as the control input, i.e., $\frac{d}{dt}(\ddot{x}_{ref}) = u$. Note that if the jerk of the cup trajectory was minimized, the resulting movement would be the same as the minimum jerk OFC model without impedance. Therefore, the acceleration of the reference trajectory was included as a state in the state vector:

$$
\begin{aligned}
(M_{arm} + M + m)\ddot{x} &= -ml\ddot{\phi} + k_p(x_{ref} - x) + k_d(\dot{x}_{ref} - \dot{x}) + F_{pert} \\
l\ddot{\phi} &= -g\phi - G\ddot{x} \\
\dddot{x}_{ref} &= u,
\end{aligned}
\tag{13}
$$

which was written in a state-space form as:

$$
\mathbf{x} = \begin{bmatrix} x,\ \phi,\ \dot{x},\ \dot{\phi},\ x_{ref},\ \dot{x}_{ref},\ \ddot{x}_{ref},\ F_{pert} \end{bmatrix}^T
$$

$$
\mathbf{A} = \begin{bmatrix}
0 & 0 & 1 & 0 & 0 & 0 & 0 & 0 \\
0 & 0 & 0 & 1 & 0 & 0 & 0 & 0 \\
\frac{-k_p}{\alpha} & \frac{mg}{\alpha} & \frac{-k_d}{\alpha} & 0 & \frac{k_p}{\alpha} & \frac{k_d}{\alpha} & 0 & \frac{1}{\alpha} \\
\frac{k_pG}{l\alpha} & \frac{-g}{l}(1 + \frac{Gm}{\alpha}) & \frac{k_dG}{l\alpha} & 0 & \frac{-k_pG}{l\alpha} & \frac{-k_dG}{l\alpha} & 0 & \frac{-G}{l\alpha} \\
0 & 0 & 0 & 0 & 0 & 1 & 0 & 0 \\
0 & 0 & 0 & 0 & 0 & 0 & 1 & 0 \\
0 & 0 & 0 & 0 & 0 & 0 & 0 & 0 \\
0 & 0 & 0 & 0 & 0 & 0 & 0 & 0
\end{bmatrix}
\tag{14}
$$

$$
\mathbf{B} = [0,\ 0,\ 0,\ 0,\ 0,\ 0,\ 1,\ 0]^T
$$

$$
\mathbf{H} = \mathbf{I}_{8\times 8}.
$$

In both minimum-jerk variants (equations 12 and 14), the state penalties $\mathbf{Q}_t$ were defined similarly as in (8) with penalty terms for cup position and velocity, as well as the ball angle.

2.2.6 Simulating Movements with a Rigid Object

All four models described in (7), (10), (12), and (14), were developed based on the cup-and-ball system. To simulate the movements with the rigid object, the states regarding the ball movement (i.e., ϕ and $\dot{\phi}$) were removed from the state vector, as well as the corresponding rows and columns from the matrices **A**, **B**, **H**, and **Q**.

2.2.7 Simulating Null, Perturbed, and Catch Trials

The experimental design tested four different trial types: null, perturbation, catch-null, and catch-perturbed. For the perturbation trials and also the null trials, prior to the onset of movement a visual cue (the speed bump or the absence of a bump) informed the subjects about the presence or absence of a perturbation. To incorporate this 'knowledge' in the simulations, the perturbation force F_{pert} was included as a state in the state-space equations; by initializing simulations with $F_{pert} = -20$ N, the knowledge about the time-dependent dynamics of the perturbation was already incorporated in the control system via the time-dependent **A** matrix. For the null trials, the perturbation state F_{pert} was set to zero. In this case, the perturbation was neither 'expected' by the controller, nor did it occur.

For the catch trials, the simulations were performed in a two-step procedure (**Fig. 3**). For catch-perturbed trials, a movement was first simulated as a null trial and then the optimal control gains were obtained ($\mathbf{L}^*$ in $u = \mathbf{L}^*\hat{\mathbf{x}}$; **Fig. 3A**; see [43]). In the second step, the movement was simulated based on the dynamics of a perturbed trial, even though the control gains were obtained from the null trial in the previous step (**Fig. 3B**). In this case, the controller was not prepared for a perturbation, but a perturbation occurred. Conversely, for the catch-null trials, the optimal control gains were first obtained by simulating a perturbed

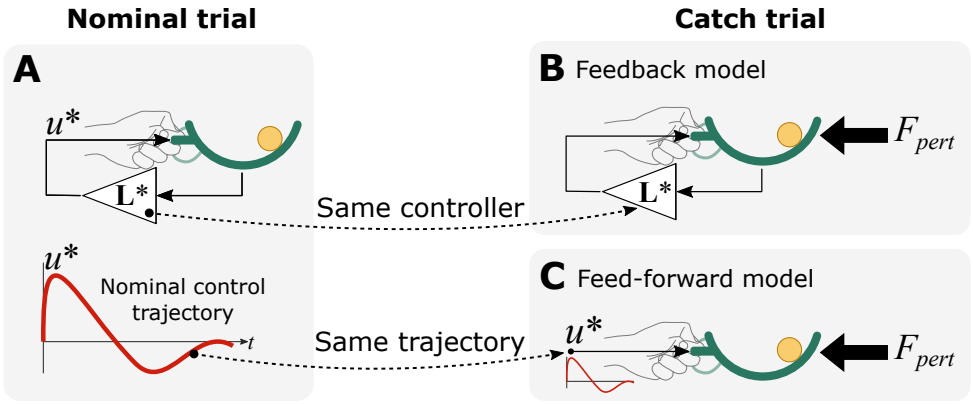

Fig 3. Simulating the catch-perturbed condition. **A**. In the nominal condition without perturbation, a nominal optimal control model was created, which expected no perturbation. **B**. To simulate the catch-perturbed trial, the same controller L^* that was unaware of the perturbation was used to simulate a trial that faced a perturbation (the *feedback-driven model*). **C**. Only the nominal control trajectory u^* was supplied to the perturbed simulation in the *feed-forward model*. The inverse procedure was used for catch-null trials, where a perturbation-aware controller was used in a trial without perturbation.

trial, and then the same control gains were used to simulate a movement based on the dynamics of a null trial. Here, the knowledge about the perturbation was incorporated in calculating the control gain, but the perturbation did not occur.

2.2.8 Simulating Feed-Forward Control

For the feed-forward simulations, the control command u was first obtained from the optimal feedback control applied to a given 'nominal' condition (e.g., for a null trial, **Fig. 3A**), and then replayed in a feed-forward manner. This controller was specifically used to simulate the catch conditions to assess how the control command without sensory feedback could compensate for unexpected perturbations.

Table 2. The list of free parameters for model fitting. The check marks indicate whether a given parameter was present in a given model.

Parameter	Bounds (lower, upper)	Min-effort		Min-jerk	
		No impedance	With impedance	No impedance	With impedance
p_x	$(10^2, 10^9)$	✓	✓	✓	✓
p_b	$(1, 10^5)$	✓	✓	✓	✓
M_{arm} (kg)	$(0, 5)$	✓	✓	N/A	✓
k_p (N/m)	$(0.1, 200)$	N/A	✓	N/A	✓
k_d (N.s/m)	$(0.1, 200)$	N/A	✓	N/A	✓
M_{ref} (kg)	$(0.05, 20)$	N/A	✓	N/A	N/A

2.3 Model Fitting

Each control model contained free parameters that were used to fit the model predictions to experimental data. The list of free parameters for each model and their lower and upper bounds are summarized in **Table 2**. All other parameters, such as for the noise terms, were fixed across all models (**Table 1**).

To fit each model, an off-line nonlinear optimization algorithm searched for the parameter values that minimized the overall error of the fit (see below) across all four experimental blocks. The models were fit to the data of each participant separately. This optimization procedure consisted of two stages. In the first stage, a global optimization process was implemented to find appropriate initial values for the parameters to be used in a more refined optimization later. This stage was implemented using the particle swarm optimization algorithm (MATLAB function `particleswarm`, MATLAB 2021a) with a maximum of 300 iterations. In the second stage, the obtained parameters were used as a starting point for a nonlinear gradient-based optimization algorithm (sequential quadratic programming, implemented with `fmincon` in MATLAB 2021a), to converge to the optimal values faster.

2.4 Model Evaluation Against Experimental Data

To compare the simulated and experimental trajectories for model fitting, all trajectories were first time-aligned based on the moment when the cup had traveled 60% of the target distance; this coincided with the perturbation onset in the perturbed trials. All experimental trajectories were re-sampled at 100 Hz to match the sampling rate of simulated trajectories. To evaluate the performance of each model, the root-mean-squared error (RMSE) between model and data was obtained for five variables: position and velocity of the cup, angular position and velocity of the ball, and the interaction force. For each variable, the model prediction was compared to the data in the last 40 trials of each block (to focus on stable performance). The resulting RMSE values were averaged and then normalized as follows:

$$e_{\square} = \frac{\frac{1}{n}\sum_{i=1}^{n}\sqrt{\frac{1}{N}\sum_{t=0}^{N}\left(\square_t^i - \square_t^{sim}\right)^2}}{\frac{1}{n}\sum_{i=1}^{n}\sqrt{\frac{1}{N-1}\sum_{t=0}^{N-1}\left(\square_t^i\right)^2}}. \tag{15}$$

where the symbol $\square$ represents the variable of interest (x, $\dot{x}$, ϕ, $\dot{\phi}$, and F_{inter}), i is the trial number (out of $n = 40$ trials in the block), and t is the time step (with total number of N steps that depended on the participant's average trial duration). The normalization intended to make the error comparable across different variables. Then, the average of these normalized errors across all variables was taken as the single evaluation measure that represented the overall modeling error for a given block and subject:

$$e = \frac{1}{5}\left(e_x + e_{\dot{x}} + e_{\phi} + e_{\dot{\phi}} + e_{F_{inter}}\right). \tag{16}$$

For the rigid-object condition, e_ϕ and $e_{\dot{\phi}}$ were removed.

2.5 Statistical Analysis of the Modeling Results

The overall modeling error in (16) was used to statistically compare the selected models. The goal was to evaluate whether the model variants resulted in statistically different predictions quantified by the model-fitting errors.

To evaluate the effect of impedance on the model behavior (Hypothesis 1), a three-way repeated-measures ANOVA was performed. The three factors were model type (with versus without impedance), object type (rigid object versus cup-and-ball), and perturbation type (null versus perturbed). The next analysis on the effects of the cost function applied a four-way repeated-measures ANOVA (Hypothesis 2). The factors were model type, object type, and perturbation type as before, as well as the cost function (minimum-effort versus minimum-jerk). Catch trials were excluded for these two analyses. Finally, to assess the effects of feedback on performance, another four-way repeated-measures ANOVA was used with the factor feedback condition (feedback versus feed-forward) instead of cost function (Hypothesis 3). Only catch trials were used in the last analysis. To disentangle the interactions, posthoc comparisons with Tukey-Kramer corrections were applied. All statistical tests were performed in Matlab 2021a, using the ANOVA tools and `multcompare` function (The Mathworks, Natick, MA).

As different models had different number of parameters, the Bayesian Information Criterion (BIC) was applied to each model. BIC evaluates the model performance based on the data fitting error, while also compensating for the number of free parameters to avoid over-fitting [50]. A BIC difference of greater than 4.6 (a Bayes factor of greater than 10) was considered as strong evidence in

favor of the model with the lower BIC value [51]:

$$\mathrm{BIC} = n \log\left(\frac{e}{n}\right) + k \log(n), \tag{17}$$

where n is the number of data points, k is the number of free parameters in the model, and e is the performance error calculated in (16).

3 Results

3.1 Behavioral Results

Participants were largely successful in all task conditions. When transporting the cup-and-ball in Blocks 3 and 4, they only lost the ball in 56 trials out of the total of 2200 trials in this condition. The median success rates across participants, i.e., percentage of trials in which the ball was not lost, were 99% and 97% in Blocks 3 and 4, respectively.

To probe whether there were improvements due to practice within each block, trial durations across the 100 trials of each block were examined. The median movement time between the first 25 and last 25 trials of each block were compared using Wilcoxon signed rank test; failed trials and catch trials were excluded. The median movement time decreased with practice only in Block 3 (unperturbed cup-and-ball condition, see **Table 3**). No significant changes in movement times were observed in other blocks. Note the significantly higher movement times in Blocks 3 and 4 when the ball was sliding inside the cup; this observation gave first evidence for the higher demands when transporting the cup with the moving ball.

Figure 4 summarizes average trajectories of cup and ball and interaction forces

Table 3. Trial durations in the four experimental blocks. Median trial durations across all participants are reported.

Block	All trials	First 25 trials	Last 25 trials	Wilcoxon signed rank test
1	1.43±0.24 s	1.45±0.44 s	1.41±0.25 s	$W = 40$, $p = 0.57$
2	1.43±0.20 s	1.45±0.23 s	1.40±0.24 s	$W = 50$, $p = 0.15$
3	1.91±0.34 s	1.97±0.37 s	1.86±0.25 s	$W = 95$, $p = 0.019$
4	1.81±0.27 s	1.83±0.23 s	1.80±0.22 s	$W = 43$, $p = 0.41$

in all conditions; catch and failed trials were excluded. Panels **A-E** show one example participant's behavior, and panels **F-J** present averages across all participants. The other individual participants' data are provided in the Supplementary Material, **Figures S-2** through **S-45**. As expected, in the rigid object condition of Blocks 1 and 2, participants moved the object to the target with kinematics that resembled those seen in free reaching, i.e., a smooth bell-shaped velocity profile (**Fig. 4A, B**, cyan trajectories). With the introduction of the ball dynamics in Blocks 3 and 4, new movement profiles emerged that were distinctively different from those in the rigid object condition. Specifically, the cup velocity (**Fig. 4B**, light brown trajectories) exhibited a 'plateau', instead of the prominent peak in the rigid object condition. These features were robustly observed across all participants, as indicated by the narrow standard deviation bands in **Fig. 4F-J**.

Prior to the onset of the predictable perturbations in Blocks 2 and 4, participants' movement patterns were similar to those in the unperturbed trials, both with the rigid object and with the cup-and-ball system (**Fig. 4**, darker brown trajectories). Until arriving at the perturbation location, participants continued to move with a velocity profile that showed a single prominent peak in the rigid object case, and a plateau in the cup-and-ball condition (**Fig. 4B, G**). In both conditions, the impulsive resistive force caused a sudden drop in the cup velocity; in the cup-and-

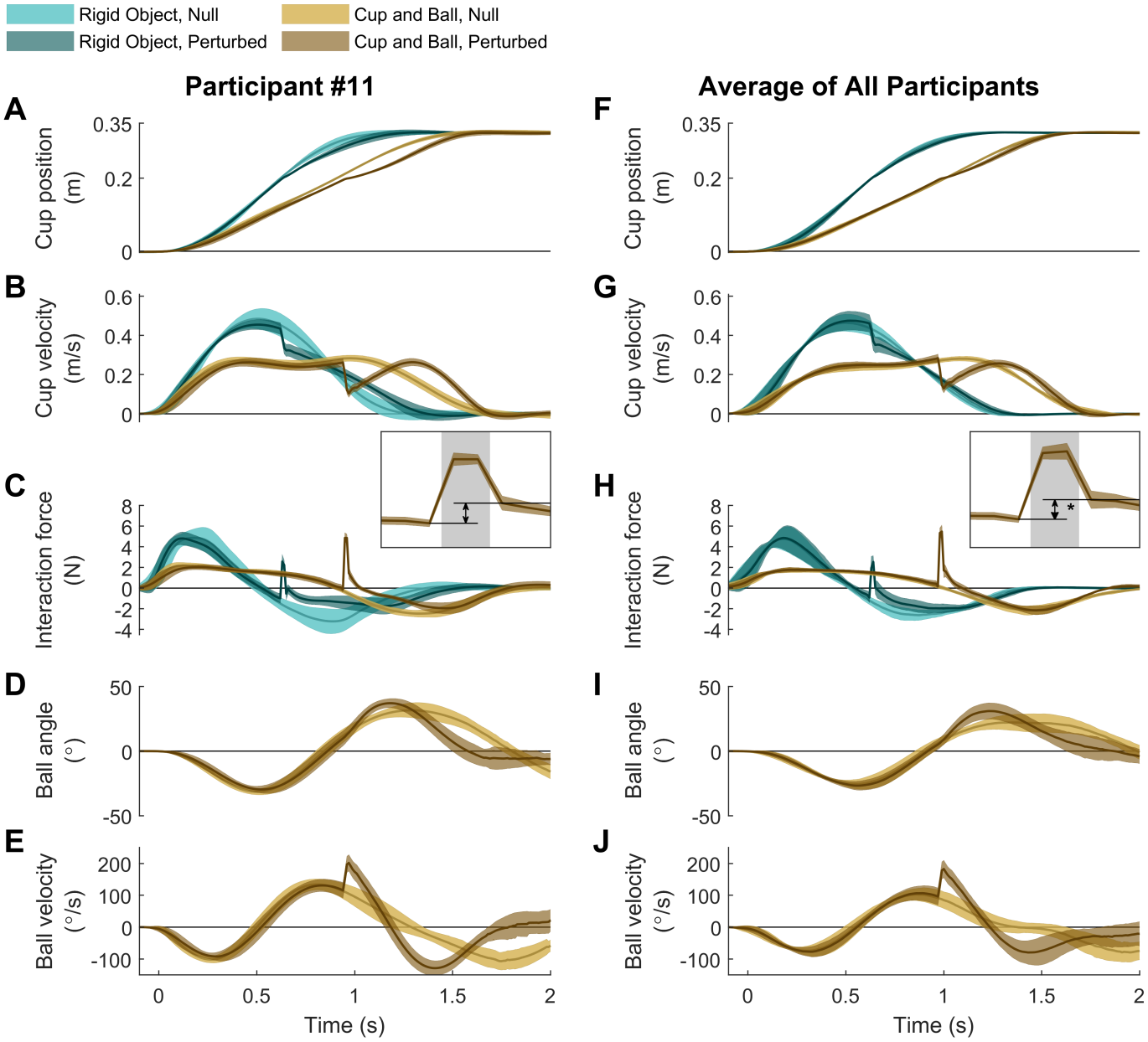

Fig 4. A-E. Example participant's trajectories with the rigid object and the cup-and-ball system, under free and perturbed conditions. Different color lines show the mean ± one standard deviation of the corresponding trajectories across trials for each block (excluding the catch trials). The inset in panel **C** highlights the detailed features of the interaction force at the perturbation in the cup-and-ball condition. The shaded region is the 20 ms interval in which the perturbation was applied. **F-J**. Summary of all participants' trajectories. Mean ± one standard deviation of the average trajectories from all participants' are shown.

ball condition, the cup velocity rebounded after the perturbation (**Fig. 4B, G**), but this rebound was absent in the rigid-object condition. Further, with both objects, the interaction force showed a prominent spike (**Fig. 4C, H**). The interaction force exhibited a 'discontinuity' at the time of perturbation as highlighted in the zoomed-in insets in **Fig. 4C, H**; the interaction force right after the perturbation was consistently larger than its value at the onset of perturbation as the inset highlights. Averaged across participants, this increase was 0.99±0.72 N with the rigid object ($t(10) = 4.553$, $p = 1.05 \times 10^{-3}$) and 1.52±0.69 N with the cup-and-ball system ($t(10) = 7.323$, $p = 2.53 \times 10^{-5}$).

3.2 Modeling the Behavior

3.2.1 The Effects of Impedance

Figure 5A, B illustrates the simulation results from the standard minimum-effort model with and without impedance, together with the experimental data for one participant. For the rigid-object condition (**Fig. 5A**), both models captured the qualitative patterns of the human movements in both perturbed and unperturbed trials. Specifically, both models produced the bell-shaped velocity profile and the velocity drop without rebound after the perturbation. However, the models differed in capturing the features of the interaction force around the perturbation. In the perturbed trials, the data showed an increase in the force level from before to after the perturbation (average across participants: 0.99 ± 0.72 N). While such sudden increase was reproduced by the model that included impedance (0.38 ± 0.33 N), the model without impedance failed to account for this behavior and instead showed a decrease in force (-0.15 ± 0.13 N).

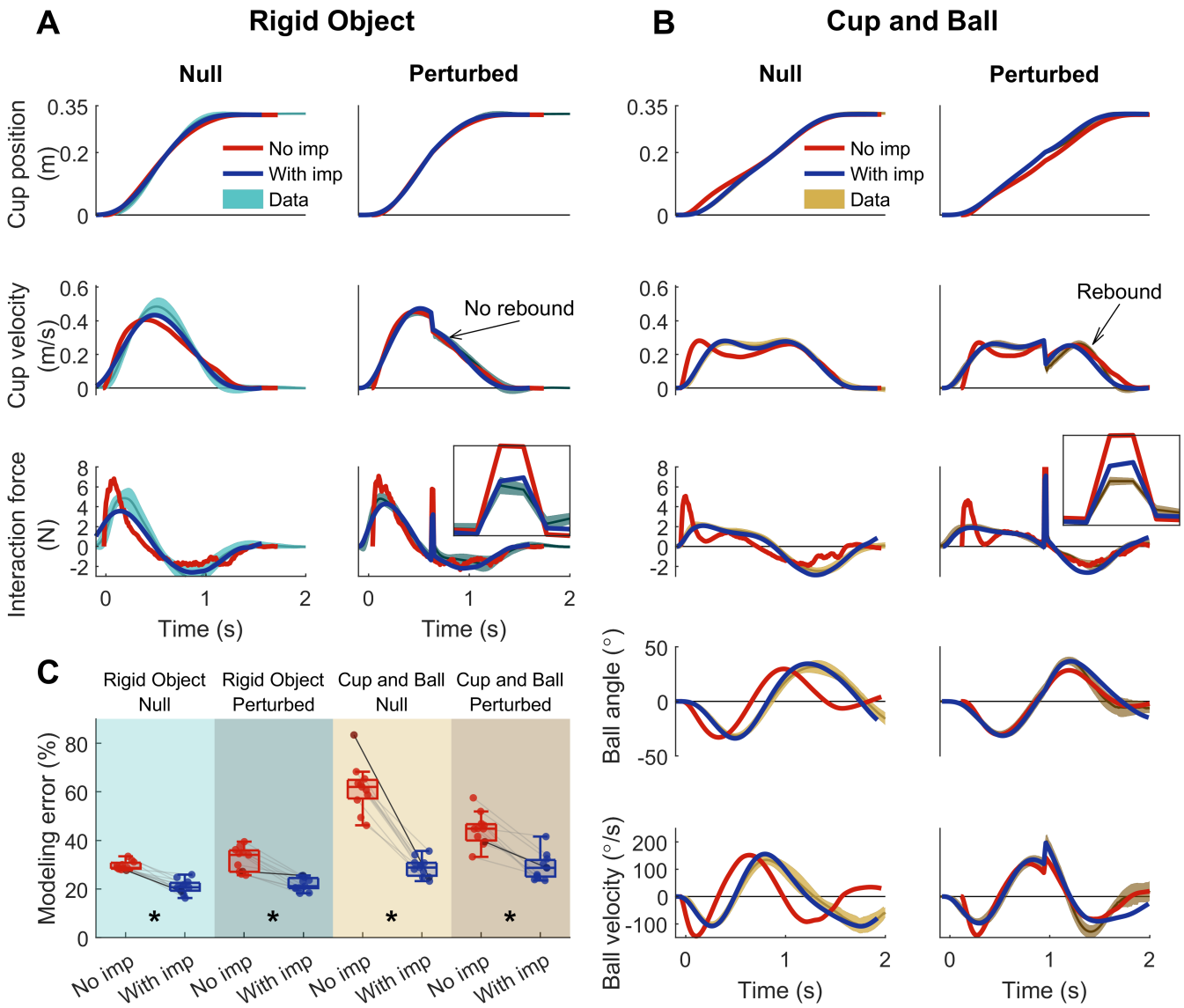

Fig 5. Comparison of the responses of the minimum-effort models against the human data. **A**. Rigid object condition. **B**. Cup-and-ball condition. Interaction forces and positions and velocities of the cup and the ball from the same exemplary participant #11 as in **Fig. 4** are shown. The shaded bands around the mean trajectories show one standard deviation. The two OFC responses (with and without impedance) are overlayed on the human data. **C**. Modeling error quantified by the mean of the normalized root-mean-squared error of all trajectories. Each pair of dots connected by a line represents the modeling of one participant. The black line belongs to participant #11.

The inclusion of the ball dynamics separated the two models' behavior further (**Fig. 5B**). Without impedance, the qualitative characteristics of the simulated

movement deviated from the human data more distinctively. In contrast, with impedance, the OFC model modulated the interaction force and consequently the cup velocity less, leading to qualitatively similar behavior as seen in the human data. Similar to the rigid-object condition, the inclusion of impedance allowed the model to reproduce the discontinuous increase in interaction force from before to after the perturbation; Averaged across participants, the simulated interaction force increased by 0.81 ± 0.54 N (human data: 1.52 ± 0.69 N). This feature could not be captured in the absence of impedance, and the interaction force decreased by -0.15 ± 0.08 N in the simulation. Another salient behavioral feature in the perturbed cup-and-ball condition was the smooth rebound of the cup velocity after the perturbation. In the face of perturbations, both models closely replicated the drop and rebound of the cup velocity as well as the spike in interaction force.

The overall error between the simulated and measured behavior was quantified using an aggregate root-mean-square error of fit that took into account the trajectories of all cup and ball states and the interaction force (**Fig. 5C**). In both null and perturbed conditions, this overall modeling error was smaller when impedance was included in the model. A three-way repeated-measures ANOVA revealed statistically significant two-way and three-way interactions and main effects. The full ANOVA results are presented in **Table S-1**. Because the goal was to compare the modeling error with and without impedance in each test condition, planned pair-wise comparisons were made within each block using Tukey-Kramer tests. Results indicated statistically significant differences between the two models in all four condition blocks ($p = 0.0016$, $p = 0.0038$, $p = 7.68 \times 10^{-5}$ and $p = 0.013$ for Blocks 1 to 4, respectively). The inclusion of impedance resulted in significantly better fit to the data in all conditions.

The models involved a number of parameters that were fitted to individual participants' data and are summarized in **Fig. 6**, and **Table 4**. Results of the BIC analyses showed that the inclusion of impedance in the model reduced BIC for all participants with a difference of $\Delta\text{BIC} > 61$, suggesting that the model with impedance proved to be a better underlying modeling structure (see details in **Fig. S-1** in the Supplementary Material). These modeling results highlighted the importance of mechanical impedance for the overall system behavior.

3.2.2 The Effects of the Objective Function

For the above analyses, both models included minimization of effort as their objective function, consistent with many previous studies [32, 46]. The following comparisons tested the influence of the objective function on the models' behavior in the context of interactions with a complex object.

In interaction with the rigid object (**Fig. 7A**), all four model variants (with or without impedance, minimizing jerk or minimizing effort) produced the expected

Table 4. Mean±standard deviation of the identified parameters, averaged across participants. Impedance's stiffness (k_p) and damping (k_d), arm mass (M_{arm}), reference trajectory's inertia (M_{ref}), and penalties on cup and ball states ($log_{10}(p_b), log_{10}(p_x)$) are reported. N/A indicates that the parameter was not included in the model.

Parameter	Min-effort		Min-jerk	
	No impedance	With impedance	No impedance	With impedance
k_p (N/m)	N/A	49.47 ± 12.08	N/A	58.92 ± 47.49
k_d (N.s/m)	N/A	9.26 ± 3.45	N/A	18.04 ± 2.96
M_{arm} (kg)	3.28 ± 1.96	0.79 ± 0.23	N/A	0.61 ± 0.14
M_{ref} (kg)	N/A	17.46 ± 2.39	N/A	N/A
$\log_{10}(p_x)$	6.45 ± 0.22	7.28 ± 0.26	6.17 ± 0.41	6.34 ± 0.50
$\log_{10}(p_b)$	2.08 ± 0.31	1.31 ± 1.16	1.91 ± 0.30	1.44 ± 0.80

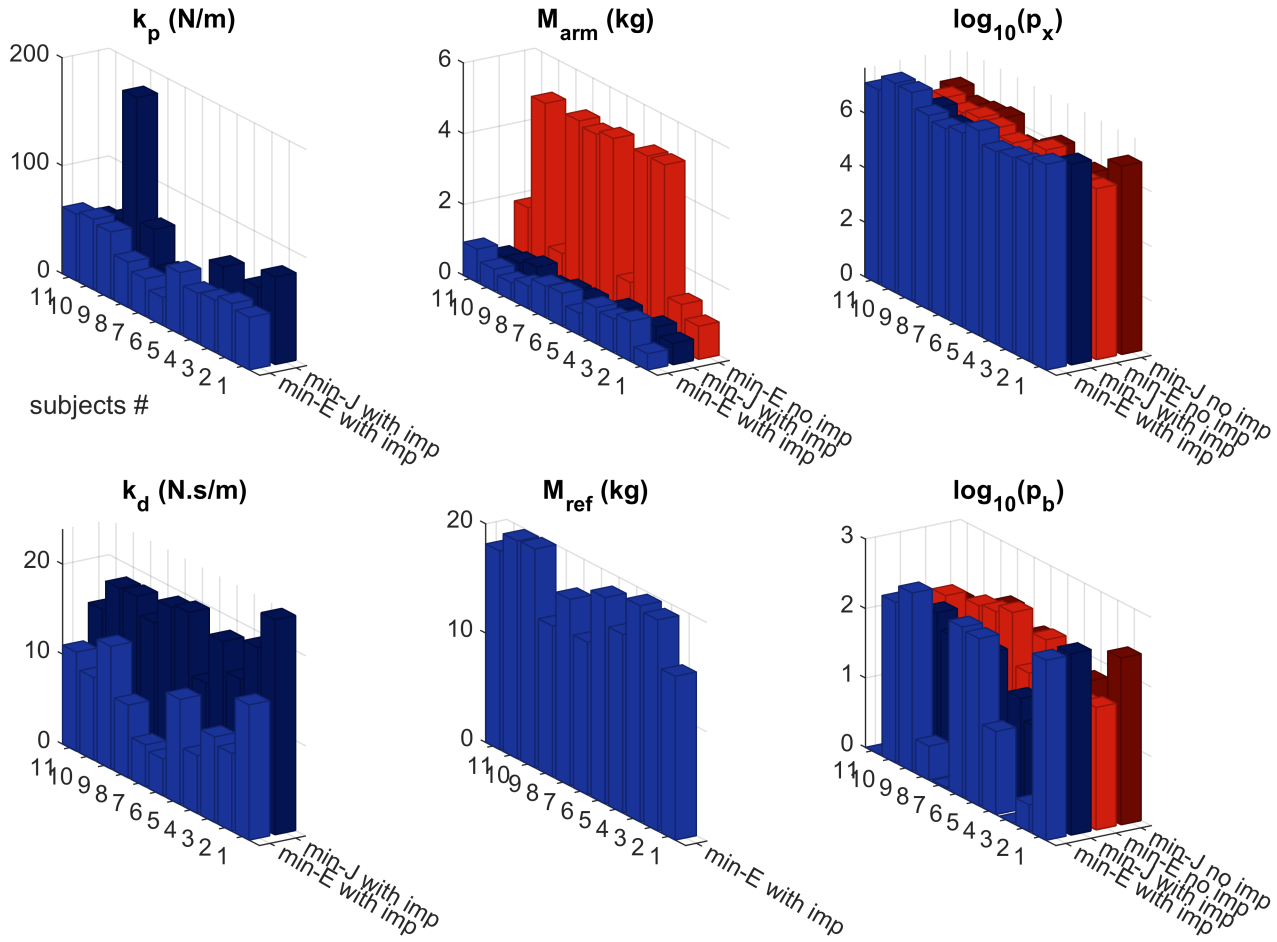

Fig 6. Model parameters fitted to each participant's data. Impedance's stiffness (k_p) and damping (k_d), arm mass (M_{arm}), reference trajectory's inertia (M_{ref}), and penalties on cup and ball states ($log_{10}(p_x), log_{10}(p_b)$) are identified. See **Table 4** for the average values.

smooth bell-shaped velocity profile. All these models, with exception of minimum-jerk without impedance, performed qualitatively similar to the human data when facing the perturbations in Block 2 (**Fig. 7B**). Note that the minimum-jerk model directly prescribed the cup kinematics and, by design, the perturbation forces in Block 2 did not affect the cup movement and did not produce the sudden velocity drop (dashed red line in **Fig. 7B**).

In contrast, in the cup-and-ball condition, the two models without impedance produced distinct movement profiles (**Fig. 7C**). The minimum-jerk model variant generated a single-peaked velocity profile, as opposed to the pronounced double-peaked profile of the minimum-effort variant (compare the solid and dashed red lines in **Fig. 7C**). However, when impedance was included, the two variants produced very similar movement patterns. Similar observations hold in the perturbed cup-and-ball condition (**Fig. 7D**): without impedance, the minimum-effort and minimum-jerk variants behaved distinctively from each other (solid and dashed red lines), while the two cost functions resulted in similar behavior when impedance was present in the model (solid and dashed blue lines).

These qualitative similarities and differences were clearly reflected in the quantitative error **Fig. 7E-F**. Without impedance, the modeling errors from the minimum-effort and minimum-jerk variants were different in all four test conditions. However, with impedance, the two objective functions resulted in comparable modeling errors. A four-way repeated-measured ANOVA compared the modeling error with the factors model type (with versus without impedance), objective function (minimum-effort versus minimum-jerk), object type (rigid object versus cup-and-ball), and perturbation type (unperturbed versus perturbed). Results revealed that the model type produced a strong main effect ($F(10) = 1069.1$, $p = 1.69 \times 10^{-11}$), while the cost function did not yield a significant main effect $F(10) = 0.010$, $p = 0.920$). Only the three-way and four-way interactions that involved model type and cost function showed statistical significance ($F(10) \geq 17.13$, $p \leq 0.002$). The full ANOVA results are presented in **Table S-2**. Planned pairwise comparisons within each test condition (**Fig. 7E-H**) showed that the error from the two model variants without impedance were different in all four

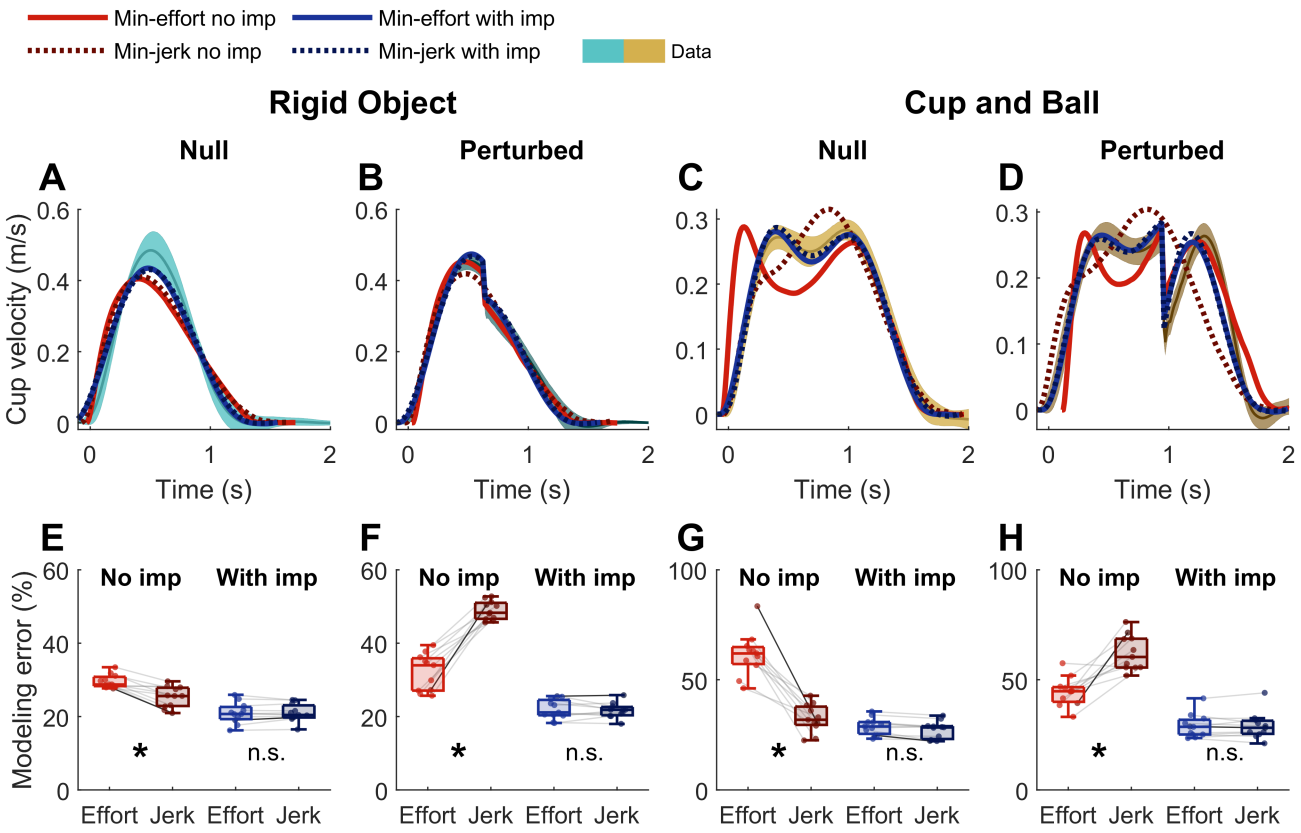

Fig 7. Effect of the objective function on model behavior. The minimum-effort and minimum-jerk criteria are compared in models with and without impedance. Panels **A-D** show the simulated cup trajectories overlaid on one example participant's data (same participant #11 as in **Fig. 4**). Panels **E-H** show quantitative comparisons of the overall modeling error across all participants. The asterisk * indicates statistically significant differences ($p < 0.05$) between the minimum-effort and minimum-jerk models, and n.s. (not significant) indicates no statistically significant differences ($p > 0.05$). Each thin line represents a participant; the solid black line belong to the shown participant.

blocks ($p \leq 0.0132$). However, with impedance, the two model variants were not statistically distinguishable in any of the blocks ($p \geq 0.195$).

3.2.3 The Effects of Sensory Feedback

To investigate the role of sensory feedback on the models' behavior, *catch* trials were analyzed. Note that catch trials were visually identical to the rest trials within the same block and there was no indication that would inform the participants about the change in the perturbation condition. These trials afforded separating the effects of pre-planning from a feedback-driven response in the face of the unexpected event.

Figure 8A-D illustrates the experimental and simulation results for both types of catch trials. Only the standard minimum-effort models were analyzed here. When sensory feedback was present, the model without impedance (solid red lines) could drive the rigid object to the target and stop there, despite the unexpected perturbation in the catch-perturbed trial (**Fig. 8A**). When sensory feedback was removed from the model (dashed red lines), the simulated cup velocity no longer reached zero velocity at the end of the trial; the cup stopped and moved back in the opposite direction with negative velocity by the end of the trial (**Fig. 8A**). Interestingly, by introducing impedance, the feedback and feed-forward control policies became similar (respectively, solid and dashed blue lines in **Fig. 8A**). Both models could recover from the unexpected perturbation and successfully transport the rigid object to the target and stop there. Similar behavior was observed in the catch-null trials (**Fig. 8B**), where the perturbation was unexpectedly removed: without impedance, the feed-forward model could not cope with the unexpected scenario. In contrast, the inclusion of impedance enabled both models, with or without sensory feedback, to successfully finish the task. The inclusion of the ball enhanced these effects, and the undershoot and overshoot of the cup velocity with the feed-forward were even more pronounced in the absence of impedance

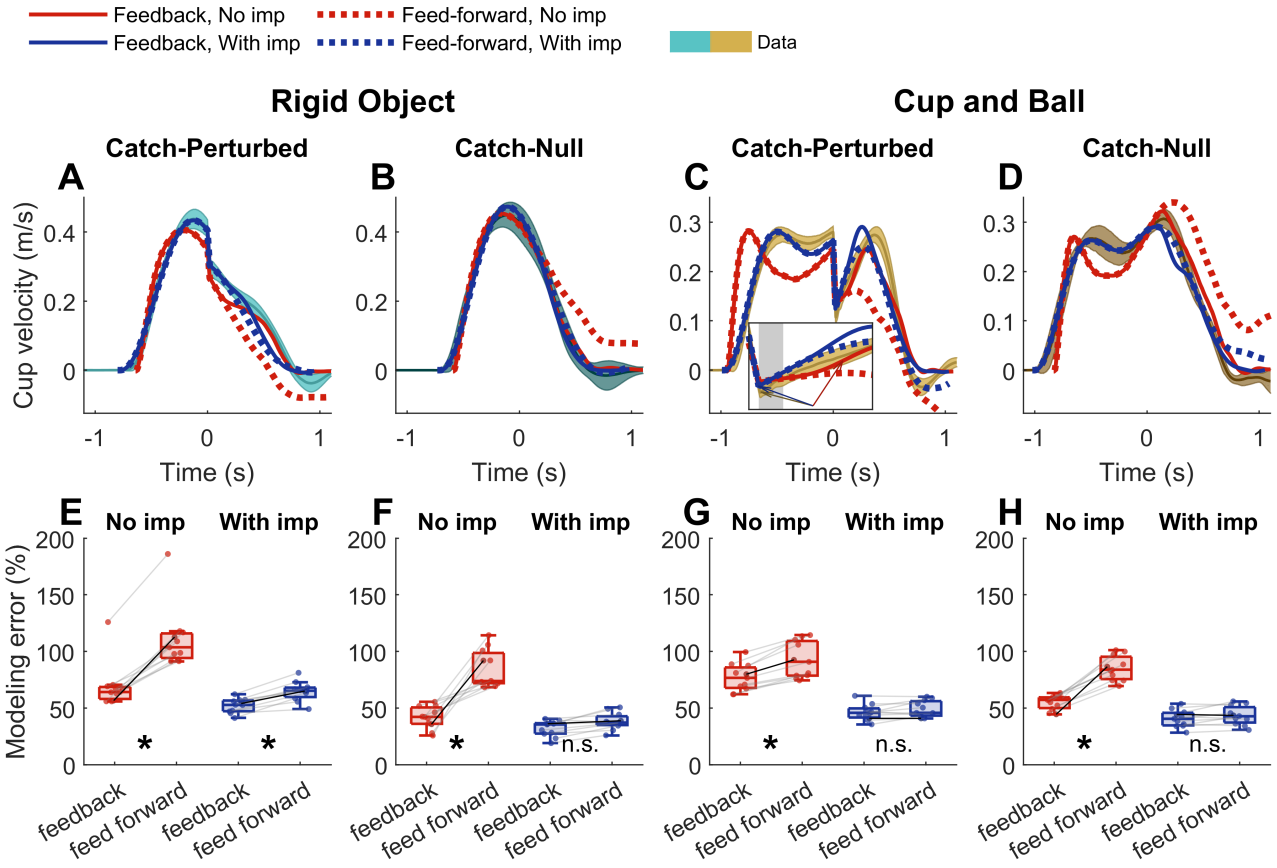

Fig 8. Catch trials to assess the effects of sensory feedback on model performance. In catch-perturbed trials, participants unexpectedly experienced a perturbation in a block where 95% were null trials. In catch-null trials the visual cue (Speed bump) alerted subjects to the upcoming perturbation as in most other trials, but no perturbation was applied. **A-D**. Experimental and simulated results for catch trials: cyan and light brown bands represent one participant's data for rigid-object and cup-and-ball conditions, respectively (same participant #11 as in **Fig. 4**). Solid lines represent the feedback model without (red) and with (blue) impedance; dashed lines represent the feed-forward replay of the nominal control trajectories in the catch trial. The inset in **C** magnifies the trajectories around the perturbation. The shaded region corresponds to 50 ms simulated sensory delay, and the arrows points to the moment of maximum cup acceleration. All time series of experimental data and simulations were aligned based on the moment when the cup arrived at the onset of perturbations, at 60% distance towards the target. **E-H** Overall error between the human data and simulation. Asterisk * indicates statistically significant differences ($p < 0.05$) between the feedback and feed-forward models; 'n.s.' indicates not significant ($p > 0.05$). Each thin line represents one participant; the solid black line belong to the participant shown above.

(**Fig. 8C, D**). Both variants with impedance, however, were successful at the task.

The rebound in the cup velocity following the perturbation (**Fig. 8C**) distinguished the models even further. Without impedance, the velocity rebound deviated from the data even when the control model utilized sensory feedback (highlighted in the inset of (**Fig. 8C**). In the data, the cup acceleration peaked immediately (within 5 ms) after the perturbation ended. Across participants, the average cup acceleration before perturbation onset was 0.15 ± 0.09 m/s^2 and rose to 1.06 ± 0.27 m/s^2 immediately (within 5 ms) after the perturbation. This instantaneous behavior was observed in all participants. However, in the absence of impedance the simulated cup acceleration did not exhibit this instantaneous rise; cup acceleration was 0.098 ± 0.091 m/s^2 and 0.072 ± 0.075 m/s^2, before and after perturbation, respectively. In this case, the controller received sensory feedback with a 50 ms delay, and could only respond to the perturbation after processing the delayed information. Consequently, the cup acceleration took 152 ± 8 ms to rise to a value that was comparable to the measured peak acceleration, i.e., within one standard deviation from the mean of the data. On the other hand, the model with impedance reproduced this instantaneous response after the perturbation, and cup acceleration peaked immediately following the perturbation and reached 0.71 ± 0.30 m/s^2 (from 0.17 ± 0.06 m/s^2 at perturbation onset). Note, that although the feed-forward model with impedance had an extra inertia parameter (M_{ref}) compared to the model with no impedance, this additional inertia cannot account for the rebound of cup velocity and acceleration after the perturbation (**Fig. 8C**). Such immediate rebound is achieved through a mechanism that can store and release energy in the face of a perturbation, which in our case is the stiffness element in the model.

To quantify and compare the error between different models, only the trajectories after the perturbation were taken into account because the feedback and feed-forward responses were identical before the perturbation. As **Fig. 8E-H** shows, without impedance, the feed-forward variant consistently under-performed the feedback-driven one in all four conditions. However, the error from the feedback and feed-forward variants of the models were comparable in the presence of impedance. A four-way repeated-measures ANOVA was used to analyze the modeling error; the four factors were model type (with versus without impedance), feedback structure (feedback versus feed-forward), object type (rigid object versus cup-and-ball), and perturbation type (catch-null versus catch-perturbed). All two-, three- and four-way interactions that involved both model type and feedback structure revealed statistical significance ($F(10) \geq 6.97$, $p \leq 0.0247$). Further, both model type and feedback structure showed strong main effects ($F(10) \geq 99.1$, $p \leq 1.66 \times 10^{-6}$). The ANOVA results are shown in the Supplementary Materials. Following these results, planned pairwise caparisons of the model variants within each block (**Fig. 8E-H**) showed that the feed-forward model without impedance under-performed the feedback one in all test conditions with statistical significance ($p \leq 5.61 \times 10^{-3}$). However, the two variants of the model with impedance were not statistically different in Blocks 2, 3 and 4 ($p \geq 0.084$); only in Block 1, the feedback model performed better that the feed-forward variant ($p = 5.80 \times 10^{-4}$).

4 Discussion

To date, numerous studies have examined the roles of the body mechanics, optimality principles, and sensory feedback for the control of voluntary goal-directed move-

ments. Typically, the experiments were carefully designed to isolate and explore the concept in question, e.g., the cost functions [25,52], mechanical impedance [5,53], or the interaction between feedback and feed-forward pathways [54,55]. The interplay between these critical elements, however, has received less attention, with only few exceptions. For instance, the interplay between sensory feedback and impedance was studied in an isometric holding task [37] and in a postural control task [56]. Common to these studies are the simplified experimental tasks to generate clear data, e.g., the *feed-forward command* could safely be assumed constant in the cited articles. However, such simplified tasks may not be rich enough to reveal the full relation between the constituent elements of motor control. Hence, the goal of this work was to study the interplay between body mechanics, optimality criteria, and sensory feedback in an experimental assay in which humans interacted with an object that introduced internal dynamics with an underactuated degree of freedom. Such movement task posed a new set of control challenges that afforded a more intricate view into control processes.

4.1 Contributions of Impedance

The body and its mechanics ('embodiment') plays a significant role in determining control, especially in more complex movements in interaction with objects and the environment. Thus, a model's prediction about the brain's role in motor control critically depends on the neuromechanical details included in the control model [57]. To address the crucial interplay of top-down control and body dynamics, this study examined OFC's predicted behavior when the model for the body was extended with a simple representation of its inherent dynamics, mechanical impedance. To evaluate the contribution of impedance, different variants of OFC were developed

and compared.

Comparison of human kinematics in object interactions with the corresponding model simulations showed that the OFC model without impedance failed to reproduce several salient features in human performance. Several results highlighted the superior performance of the model that included impedance. First, the model with impedance produced kinematic profiles that deviated significantly less from the experimental trajectories, as quantified by the aggregate RMS error (**Fig. 5C**). Second, in the absence of impedance the simulations could not reproduce the sudden increase in the interaction force immediately following the perturbation, which was a robust feature in the human data. Third, without impedance the model's response showed a noticeable delay to an unexpected perturbation due to the 50-ms sensory delay in the model (**Fig. 8C**). No such delay was observed in the human data. However, when an impedance element was included, the model captured the subjects' overall movement profiles to a significantly greater degree. The impedance element acted as an energy buffer, allowing the model to capture the discontinuity in the interaction forces following a perturbation. Impedance also allowed the model to replicate the instantaneous response to unexpected perturbations.

The two phenomena at the perturbation, the change in interaction force and acceleration post-perturbation, occurred at a very fast timescale (< 20 ms). Neither voluntary, nor involuntary neural responses could be generated at such timescales. For comparison, the fastest stretch reflex in upper extremities only starts 20-50 ms after perturbation onset [58]. These observations imply that the instantaneous responses should be attributed to the biomechanics of the arm. Within the 20 ms duration of the impulsive perturbation force, the cup velocity decreased

significantly, while the cup position and also the position and velocity of the impedance's 'zero-force trajectory' changed only negligibly. The drop in the cup's velocity caused a sudden increase in the damping force and, ultimately, an increase in the interaction force. The same instantaneous rise in interaction force was also the reason for the immediate rebound of cup velocity after the unexpected perturbation. The model without impedance lacked this mechanical contribution, and the velocity could accelerate and rebound only after processing the delayed feedback to command an increase in muscle force.

The impedance included in the model consisted of a pair of linear and constant spring and damper elements. Despite this simple design, the model clearly outperformed the one without impedance. In reality, however, nonlinear muscle, joint, and inter-limb mechanics contribute to the effective impedance of the limb, resulting in stiffness values that vary with posture [24,59] or with the evolving movement [60,61]. Accurate representation of mechanical impedance is crucial to 'peel back' the mechanics of the body and reveal the descending commands [62–65]. In addition to the passive contributions of the musculoskeletal properties, task-dependent modulation of stiffness has also been proposed as a means of control [5, 66, 67]. The effects of time-varying modulation of impedance have been studied in musculoskeletal simulations [56, 68–70] and in robot control [71]. Results suggested that the brain may indeed use impedance-modulation as another control mechanism. However, it remains a challenge to parse the contributions of active stiffness modulation from the variations caused by the passive mechanics of the body, due to the persistent challenges of estimating time-varying impedance *in vivo* [72]. To avoid unnecessary complications and assumptions, the simple time-invariant model was adopted that still described the human data remarkably well.

The behavior of the models critically depended on the parameter values used in the simulations. Although the models were highly simplified compared to the human physiology, the lumped parameter values can be discussed in relation to biomechanical properties of the body. The identified impedance parameters were within the range of previously reported values for the end-point (hand) impedance, although the range reported in the literature spans one order of magnitude. The estimated end-point stiffness in the literature ranged from 40 N/m [73, 74] to 200 N/m [10] during rhythmic movements, and > 250 N/m [59, 75] and > 60 N/m [76] in isometric holding tasks where short-range stiffness was a major contributor. In comparison, the end-point stiffness identified via matching the model to the experimental data in our work was 49 ± 12 N/m and 59 ± 47 N/m in the minimum-effort and minimum-jerk models, respectively. Likewise, our estimated damping was 9.3 ± 3.4 N.s/m and 18 ± 3 N.s/m in the two models, which were within the range of $10 - 50$ N.s/m reported in [10, 73–75].

In the models that included impedance, the mass of the arm M_{arm} represented the effective inertia after the impedance element; it was estimated to be 0.78 ± 0.23 kg (minimum-effort) and 0.61 ± 0.14 kg (minimum-jerk), which was slightly higher than the mass of the hand (on average 0.5-0.6% of body mass [77], approximately 0.3-0.55 kg). This consistency can be explained by noting that forearm and upper arm partly contributed to the effective post-impedance inertia. In the absence of impedance, the identified $M_{arm} was 3.3 \pm 2.0$ kg which was close to the total mass of the arm (4.2-4.7% of body mass [77], 2.5-4.3 kg). The lumped parameter $M_{ref} = 17 \pm 2$ kg obtained when fitting the data was much larger than that of the arm. This could be physiologically realistic because this parameter represented the effective inertia of all force-producing machinery in the body. This

effective inertia might include the contributions of trunk and even leg muscles, as it is not unreasonable to assume that core muscles also engage in responding to perturbations, hence, leading to a relatively larger inertia value for M_{ref}.

Not only did the added mechanical impedance replicate human movements much better, it also provided further important insights about two cornerstones of optimal feedback control: 1) Detailed features of the cost function became less important when impedance was added. 2) Sensory feedback for the processing of error and correction became less critical. These two issues will be discussed next.

4.2 Contributions of the Cost Function

To answer *why* a certain movement pattern is chosen over possible alternatives, the cornerstone of optimal control theory is that the controller, or the brain, seeks to minimize a certain objective function. In movement neuroscience, there has been considerable debate which objective function the brain is trying to optimize (see [25] for a review). A multitude of objective functions have been proposed, ranging from the kinematics-based objectives (e.g., minimum jerk [26,29], crackle [27], and acceleration [28]), to the kinetics-based ones (e.g., minimum torque change [33] and muscle effort [30, 32]), to the minimum variance cost [31], and the physiological energy expenditure [34, 35]. All of these objectives were able to describe human movements reasonably well in their respective experimental contexts. Support for any of these objectives typically involved comparing them against other objectives for a given task and then choosing the one that better matched the data. In this paper, the comparisons made between the two OFC variants with two different objective functions, effort and jerk, also displayed distinct differences in the movement patterns. Strikingly though, when impedance

was included in the controller, no quantifiable differences were observed, and both cost functions replicated the human behavior equally well. This finding suggests that, when OFC included even minimal biomechanical features, details of the objective function may become inconsequential. In the same spirit, Diedrichsen and colleagues have shown that under the assumption of signal-dependent noise, the objective of reducing effort is equivalent to reducing end-point variance [46]. Similarly, Wong and colleagues [35] showed that smooth movements are more energy efficient due to the cost of calcium ion transport in the cell membrane. Here, it is shown that the physiologically realistic element of arm impedance masks distinctions between effort and smoothness. One important implication is that the underlying control principles of the brain may be fundamentally unobservable due to the filtering effects of the body mechanics. However, it needs to be kept in mind that this finding was obtained in the context of interactions with a complex object. To what degree this blurring of details holds for other tasks requires more investigation.

4.3 Contributions of Sensory Feedback

Features of feed-forward (pre-planned) and feedback (online corrections) control mechanisms are intertwined in coordinated human movement. Following Woodworth in 1899, numerous authors have distinguished a ballistic (feed-forward) and a homing-in phase followed by error corrections (feedback) in simple pointing movements [36, 78]. In more recent years, Crevecoeur and colleagues [37] argued that feedback control was necessary to complement a feed-forward command to replicate the human response to perturbations in an isometric task. Conversely, Yeo and colleagues showed that when sensory information was uncertain, human

movements could not be explained by feedback control alone and feed-forward pathways were necessary [38]. Even in tasks that heavily rely on continuous sensory information, such as balancing a stick on the fingertip, there are compelling arguments for intermittent episodes of feed-forward predictive control [79].

This study used a dynamically complex task where the underactuated object created perturbations depending on the hand's actions. In addition to expected perturbations, unexpected perturbations in the catch trials were given to identify the role of sensory feedback. The simulations of the catch trials without an impedance element showed that the feed-forward replay of the OFC's control command was unable to cope with the perturbations or their unexpected absence. This behavior did not match the subjects' behavior (**Fig. 8**). On the other hand, the feedback-driven OFC model achieved a better fit to the data with significantly smaller model error. Based on these results, one may readily conclude that a feedback loop is necessary. However, when the model included impedance, both the feedback and feed-forward variants replicated the experimental data equally well. These findings showed that mechanical effects may have intricate contributions to coping with complex events. Even a task that involves underactuated dynamics and challenging requirements, e.g., responding to the disturbance without 'spilling the coffee', may be achieved by a feed-forward control scheme, as long as it is mediated by body mechanics.

It must be noted that our results do not simply provide support for either feed-forward or feedback control. Instead, the key insight from these results is that, under biomechanically more plausible assumptions, the distinction between predictive feed-forward and sensory-driven feedback control may become less apparent. Similar effects were reported previously in a simple reaching task by

Berret and Jean [69], who showed that attenuation of task-dependent errors could be achieved by a feed-forward tuning of the arm impedance. It should also be noted that these results must be interpreted in the context of the chosen experimental task. It is obvious that large enough and long enough perturbations can disrupt the movement to a degree that requires sensory-driven corrections, both in terms of long-latency reflexes and voluntary responses. Indeed, Crevecoeur and colleagues [37] showed that optimal feedback corrections were necessary to complement mechanical impedance after large perturbations in a holding task. However, given that arm impedance is nonlinear, e.g., exhibits short-range stiffness [80, 81], and that it changes with postural configuration [82] and movement [60,61], great care is needed when searching for the 'control structure' using perturbations. New computational techniques that simultaneously model feedback and feed-forward pathways as developed in a recent study may provide new insights [56].

4.4 Role of Impedance: Two Perspectives

From a mathematical perspective, the impedance element in the model introduced three additional states to the dynamics of the system that the optimal feedback controller had to address. However, unlike inertial mechanics that can also increase the number of states, e.g., in multi-segment arm models, impedance endows the system with potential energy storage and dissipation properties. These properties could not be achieved with inertial mechanics alone. The implications of this physical and mathematical change in the system can be interpreted from two different perspectives.

4.4.1 Brain Controls the Body

A first position puts priority to the fact that the brain is the site of control and the body is the system to be controlled. Thus, the brain as the sole control authority is fully responsible for defining the characteristics of the movements based on knowledge about the body. Grounded in this dualistic viewpoint, much of neuroscience has tried to shed light on the neural representations and neural activity patterns for the generation of movements. The search for the 'control signals' in the primary motor or parietal cortices that directly correlate with the behavior at the single-neuron [83] or population level [84, 85] follows this basic position, if not philosophically, then at least practically. To facilitate this search, the movements themselves have been held simple to allow many repetitions under the 'same' conditions and also to eliminate any interactive effects from the environment. Many studies on intracortical data in non-human primates have adopted such simple center-out reaching [83, 84] or cranking tasks [86]. While intriguing insights have been gained, interactions with an object and the environment would present a step up, not only in complexity, but also in conceptual terms. Our focus on the interaction with a dynamical object indicates that the physical properties of the body may present important challenges to the interpretability of purely top-down perspectives. Concretely, following our results, issues whether incoming sensory information affected the behavior or not, and whether the cost function was effort or smoothness became blurred by adding simple biomechanical elements. In light of these findings it becomes evident that specific facets of control might be 'filtered out' by the dynamics of the body.

4.4.2 Brain and Body Work Together

In a second view, innate dynamical properties of the body, such as mechanical impedance, are interpreted as a lower-level autonomous control authority that shares the control responsibility with the higher-level information processors. Thus, this embodiment of control means that not all characteristics of observable behavior can be attributed to the higher-level controller. The significance of the innate passive dynamics for producing movements was strikingly demonstrated in a series of passive walkers [87, 88]. These non-actuated mechanical linkages could produce stable gaits in the absence of any motors, sensors, or a 'brain'. Passive interactions of the body with a complex environment could even allow a dead fish to swim upstream [89].

Undeniably, functional human behavior is richer than these passive movements, and bodily mechanics alone cannot generate the full spectrum of functionally specific behavior. Hence, descending neural commands need to be sensitively interfaced to not only account for, but also leverage bodily mechanics. The physical properties of the body provide useful resources for embodied computation for both perception and action. 'Morphological computation' for guided actions are well studied in animals. For instance, a housefly's compound eyes can afford complex navigation skills using simple visuomotor circuitry [90], and the biomechanics of a goat's hoof enables localized slip control in rough terrains [91]. Similarly in humans, it has been demonstrated that joint compliance plays a significant role in accurate haptic perception: correct tuning of stiffness largely simplifies the computational load during control of movement [92]. In the present results, mechanical impedance of the arm proved capable of negotiating the unexpected perturbations in a feedback-deprived control scheme, highlighting the possibility of

producing 'intelligent' responses through morphological or embodied computation.

Further, physical processes on multiple scales, ranging from passive muscle force enhancement via titin proteins [93] to limb inertial mechanics, provide means to distribute control authority across the body, thereby alleviating some of the computational burden on the brain. In human movement neuroscience, only few approaches have placed emphasis on the dynamics emerging from the interplay between control and the dynamics of the body. From a neurophysiological perspective, the equilibrium point hypothesis aimed to reveal how the central nervous system specifies lambda, the equilibrium or reference configuration of a limb, via tuning of the phasic and tonic stretch reflexes [22]. From a mechanical perspective, a number of studies have demonstrated the tuning of impedance during movement [5, 67]. Further, studies on bimanual coordination have detailed how rhythmically moving limbs self-organize into autonomous nonlinear oscillators that synchronize into stable phase relations, without requiring detailed top-down control [94, 95]. Hence, movements may be the emerging response of the body leveraging the environment with simple motor commands [96]. However, to date, these approaches have been limited to simple tasks. In order to advance one step further, this study employed optimal feedback control as a high-level controller that guides the behavior of the low-level dynamics as a way to reconcile the duality between information-processing of the brain and embodiment. Such interfacing ultimately shapes the final behavior.

4.5 Conclusions

This study highlighted the importance of mechanical impedance of the body in modeling human movements. The experimental assay was humans transporting a

complex object with underactuated dynamics. Even the simple linear transport revealed that the unactuated degree of freedom required more than a bell-shaped velocity profile of the hand, quintessential in reaching or transporting a rigid body. Without a regard for the compliance of the body, an information processing OFC model fell short of reproducing characteristic features of human movements; a successful optimal feedback controller necessitated 'embodiment' (mechanical impedance) in the control loop. Perturbation trials further revealed that impedance buffered the energy and thereby obviated the need for feedback in the optimal controller. Including impedance into the model also blurred the distinction between cost functions previously suggested for various reaching tasks. Taken together, our results emphasize that attention must be given to body mechanics to better understand the controller. The results highlight the formidable challenge to gain insights into the neural controller due to its tight intertwining with the body's and the task's dynamics.

5 Acknowledgments

The research was funded by the National Science Foundation, NSF-NRI-1637854, NSF-M3X-1825942, and the National Institutes of Health, NIH-R37-HD087089 and NIH-R01-CRCNS-NS120579 (awarded to Dagmar Sternad). Reza Sharif Razavian was also funded by NSERC Postdoctoral Fellowship PDF-532835-2019. The authors also thank Mr. Piet Lammertse for continued technical assistance, and Dr. Frédéric Crevecoeur [47] for providing the open-source codes for OFC implementation in MATLAB.

References

1. Åström KJ, Torsten B. Numerical Identification of Linear Dynamic Systems from Normal Operating Records. IFAC Proceedings Volumes. 1965;2(2):96–111. doi:10.1016/S1474-6670(17)69024-4.

2. Åström KJ, Eykhoff P. System identification—A survey. Automatica. 1971;7(2):123–162. doi:10.1016/0005-1098(71)90059-8.

3. Shadmehr R, Mussa-Ivaldi F. Adaptive representation of dynamics during learning of a motor task. The Journal of Neuroscience. 1994;14(5):3208–3224. doi:10.1523/JNEUROSCI.14-05-03208.1994.

4. Krakauer JW, Pine ZM, Ghilardi MF, Ghez C. Learning of visuomotor transformations for vectorial planning of reaching trajectories. Journal of Neuroscience. 2000;20(23):8916–8924. doi:10.1523/jneurosci.20-23-08916.2000.

5. Burdet E, Osu R, Franklin DW, Milner TE, Kawato M. The central nervous system stabilizes unstable dynamics by learning optimal impedance. Nature. 2001;414(6862):446–449. doi:10.1038/35106566.

6. Haar S, van Assel CM, Faisal AA. Motor learning in real-world pool billiards. Scientific Reports. 2020;10(1):20046. doi:10.1038/s41598-020-76805-9.

7. Haar S, Faisal AA. Brain Activity Reveals Multiple Motor-Learning Mechanisms in a Real-World Task. Frontiers in Human Neuroscience. 2020;14(September):1–11. doi:10.3389/fnhum.2020.00354.

8. Sternad D, Duarte M, Katsumata H, Schaal S. Bouncing a ball: Tuning into dynamic stability. Journal of Experimental Psychology: Human Perception and Performance. 2001;27(5):1163–1184. doi:10.1037/0096-1523.27.5.1163.

9. Nasseroleslami B, Hasson CJ, Sternad D. Rhythmic manipulation of objects with complex dynamics: predictability over chaos. PLoS Computational Biology. 2014;10(10). doi:10.1371/journal.pcbi.1003900.

10. Maurice P, Hogan N, Sternad D. Predictability, force, and (anti)resonance in complex object control. Journal of Neurophysiology. 2018;120(2):765–780. doi:10.1152/jn.00918.2017.

11. Krotov A, Russo M, Nah M, Hogan N, Sternad D. Motor control beyond reach—how humans hit a target with a whip. Royal Society Open Science. 2022;9(10). doi:10.1098/rsos.220581.

12. Nah MC, Krotov A, Russo M, Sternad D, Hogan N. Dynamic primitives facilitate manipulating a whip. In: 2020 8th IEEE RAS/EMBS International Conference for Biomedical Robotics and Biomechatronics (BioRob). IEEE; 2020. p. 685–691. Available from: `https://ieeexplore.ieee.org/document/9224399/`.

13. Guang H, Bazzi S, Sternad D, Hogan N. Dynamic primitives in human manipulation of non-rigid objects. Proceedings - IEEE International Conference on Robotics and Automation. 2019;2019-May:3783–3789. doi:10.1109/ICRA.2019.8793687.

14. Nayeem R, Bazzi S, Sadeghi M, Hogan N, Sternad D. Preparing to move: Setting initial conditions to simplify interactions with

complex objects. PLOS Computational Biology. 2021;17(12):e1009597. doi:10.1371/journal.pcbi.1009597.

15. Bazzi S, Ebert J, Hogan N, Sternad D. Stability and predictability in human control of complex objects. Chaos. 2018;28(10). doi:10.1063/1.5042090.

16. Bazzi S, Sternad D. Robustness in Human Manipulation of Dynamically Complex Objects Through Control Contraction Metrics. IEEE Robotics and Automation Letters. 2020;5(2):2578–2585. doi:10.1109/LRA.2020.2972863.

17. Hogan N. An organizing principle for a class of voluntary movements. The Journal of Neuroscience. 1984;4(11):2745–2754. doi:10.1523/JNEUROSCI.04-11-02745.1984.

18. Hogan N. Contact and Physical Interaction. Annual Review of Control, Robotics, and Autonomous Systems. 2022;5(1):1–25. doi:10.1146/annurev-control-042920-010933.

19. Rancourt D, Hogan N. Stability in force-production tasks. Journal of Motor Behavior. 2001;33(2):193–204. doi:10.1080/00222890109603150.

20. Hogan N, Sternad D. Dynamic primitives of motor behavior. Biological Cybernetics. 2012;106(11-12):727–739. doi:10.1007/s00422-012-0527-1.

21. Hogan N, Sternad D. Dynamic primitives in the control of locomotion. Frontiers in Computational Neuroscience. 2013;7(MAY):1–16. doi:10.3389/fncom.2013.00071.

22. Feldman AG. Once More on the Equilibrium-Point Hypothesis (λ Model) for Motor Control. Journal of Motor Behavior. 1986;18(1):17–54. doi:10.1080/00222895.1986.10735369.

23. Latash ML. Virtual trajectories, joint stiffness, and changes in the limb natural frequency during single-joint oscillatory movements. Neuroscience. 1992;49(1):209–220. doi:10.1016/0306-4522(92)90089-K.

24. Gomi H, Kawato M. Human arm stiffness and equilibrium-point trajectory during multi-joint movement. Biological Cybernetics. 1997;76(3):163–171. doi:10.1007/s004220050329.

25. Todorov E. Optimality principles in sensorimotor control. Nature Neuroscience. 2004;7(9):907–915. doi:10.1038/nn1309.

26. Flash T, Hogan N. The coordination of arm movements: an experimentally confirmed mathematical model. The Journal of Neuroscience. 1985;5(7):1688–1703. doi:10.1523/JNEUROSCI.05-07-01688.1985.

27. Dingwell JB, Mah CD, Mussa-Ivaldi FA. Experimentally confirmed mathematical model for human control of a non-rigid object. Journal of Neurophysiology. 2004;91(3):1158–1170. doi:10.1152/jn.00704.2003.

28. Leib R, Karniel A. Minimum acceleration with constraints of center of mass: a unified model for arm movements and object manipulation. Journal of Neurophysiology. 2012;108(6):1646–1655. doi:10.1152/jn.00224.2012.

29. Svinin M, Goncharenko I, Kryssanov V, Magid E. Motion planning strategies in human control of non-rigid objects with internal degrees of

freedom. Human Movement Science. 2019;63(December 2018):209–230. doi:10.1016/j.humov.2018.12.004.

30. Ronsse R, Wei K, Sternad D. Optimal control of a hybrid rhythmic-discrete task: The bouncing ball revisited. Journal of Neurophysiology. 2010;103(5):2482–2493. doi:10.1152/jn.00600.2009.

31. Harris CM, Wolpert DM. Signal-dependent noise determines motor planning. Nature. 1998;394(6695):780–784. doi:10.1038/29528.

32. Todorov E, Jordan MI. Optimal feedback control as a theory of motor coordination. Nature Neuroscience. 2002;5(11):1226–1235. doi:10.1038/nn963.

33. Uno Y, Kawato M, Suzuki R. Formation and control of optimal trajectory in human multijoint arm movement. Biological Cybernetics. 1989;61(2):89–101. doi:10.1007/BF00204593.

34. Anderson FC, Pandy MG. Dynamic Optimization of Human Walking. Journal of Biomechanical Engineering. 2001;123(5):381. doi:10.1115/1.1392310.

35. Wong JD, Cluff T, Kuo AD. The energetic basis for smooth human arm movements. eLife. 2021;10. doi:10.7554/eLife.68013.

36. Woodworth RS. Accuracy of voluntary movement. The Psychological Review: Monograph Supplements. 1899;3(3):i–114. doi:10.1037/h0092992.

37. Crevecoeur F, Scott SH. Beyond Muscles Stiffness: Importance of State-Estimation to Account for Very Fast Motor Corrections. PLoS Computational Biology. 2014;10(10):e1003869. doi:10.1371/journal.pcbi.1003869.

38. Yeo SH, Franklin DW, Wolpert DM. When optimal feedback control is not enough: feedforward strategies are required for optimal control with active sensing. PLOS Computational Biology. 2016;12(12):e1005190. doi:10.1371/journal.pcbi.1005190.

39. Abbs JH, Gracco VL. Control of complex motor gestures: orofacial muscle responses to load perturbations of lip during speech. Journal of Neurophysiology. 1984;51(4):705–723. doi:10.1152/jn.1984.51.4.705.

40. Todorov E, Jordan MI. A Minimal Intervention Principle for Coordinated Movement. In: Advances in Neural Information Processing Systems: Proceedings of the 2002 Conference; 2002. p. 27–34. Available from: http://papers.nips.cc/paper/2195-a-minimal-intervention-principle-for-coordi.

41. Mayer HC, Krechetnikov R. Walking with coffee: Why does it spill? Physical Review E. 2012;85(4):046117. doi:10.1103/PhysRevE.85.046117.

42. Han J. A Study on the Coffee Spilling Phenomena in the Low Impulse Regime. Achievements in the Life Sciences. 2016;10(1):87–101. doi:10.1016/j.als.2016.05.009.

43. Todorov E. Stochastic optimal control and estimation methods adapted to the noise characteristics of the sensorimotor system. Neural Computation. 2005;17(5):1084–1108. doi:10.1162/0899766053491887.

44. Sohn WJ, Nayeem R, Zuzarte I, Hogan N, Sternad D. Control of Complex Objects: Challenges of Linear Internal Dynamics. In: 2020 8th IEEE RAS/EMBS International Conference for Biomedical Robotics and

Biomechatronics (BioRob). IEEE; 2020. p. 1229–1235. Available from: https://ieeexplore.ieee.org/document/9224336/.

45. van der Linde RQ, Lammertse P. HapticMaster – a generic force controlled robot for human interaction. Industrial Robot: An International Journal. 2003;30(6):515–524. doi:10.1108/01439910310506783.

46. Diedrichsen J, Shadmehr R, Ivry RB. The coordination of movement: optimal feedback control and beyond. Trends in Cognitive Sciences. 2010;14(1):31–39. doi:10.1016/j.tics.2009.11.004.

47. Crevecoeur F, Scott SH, Cluff T. Robust Control in Human Reaching Movements: A Model-Free Strategy to Compensate for Unpredictable Disturbances. The Journal of Neuroscience. 2019;39(41):8135–8148. doi:10.1523/JNEUROSCI.0770-19.2019.

48. Svinin M, Goncharenko I, Zhi-Wei Luo, Hosoe S. Reaching movements in dynamic environments: how do we move flexible objects? IEEE Transactions on Robotics. 2006;22(4):724–739. doi:10.1109/TRO.2006.878794.

49. Bazzi S, Sternad D. Human control of complex objects: towards more dexterous robots. Advanced Robotics. 2020;34(17):1137–1155. doi:10.1080/01691864.2020.1777198.

50. Schwarz G. Estimating the Dimension of a Model. The Annals of Statistics. 1978;6(2). doi:10.1214/aos/1176344136.

51. Kass RE, Raftery AE. Bayes Factors. Journal of the American Statistical Association. 1995;90(430):773. doi:10.2307/2291091.

52. Wolpert DM, Ghahramani Z, Jordan MI. Are arm trajectories planned in kinematic or dynamic coordinates? An adaptation study. Experimental Brain Research. 1995;103(3):460–470. doi:10.1007/BF00241505.

53. Selen LPJ, Franklin DW, Wolpert DM. Impedance Control Reduces Instability That Arises from Motor Noise. Journal of Neuroscience. 2009;29(40):12606–12616. doi:10.1523/JNEUROSCI.2826-09.2009.

54. Maeda RS, Gribble PL, Pruszynski JA. Learning New Feedforward Motor Commands Based on Feedback Responses. Current Biology. 2020;30(10):1941–1948. doi:10.1016/j.cub.2020.03.005.

55. Maeda RS, Gribble PL, Pruszynski JA. Learning New Feedforward Motor Commands Based on Feedback Responses. Current Biology. 2020;30(10):1941–1948. doi:10.1016/j.cub.2020.03.005.

56. Van Wouwe T, Ting LH, De Groote F. An approximate stochastic optimal control framework to simulate nonlinear neuro-musculoskeletal models in the presence of noise. PLOS Computational Biology. 2022;18(6):e1009338. doi:10.1371/journal.pcbi.1009338.

57. Pinter IJ, van Soest AJ, Bobbert MF, Smeets JBJ. Conclusions on motor control depend on the type of model used to represent the periphery. Biological Cybernetics. 2012;106(8-9):441–451. doi:10.1007/s00422-012-0505-7.

58. Pruszynski JA, Scott SH. Optimal feedback control and the long-latency stretch response. Experimental Brain Research. 2012;218(3):341–359. doi:10.1007/s00221-012-3041-8.

59. Perreault E, Kirsch R, Crago P. Effects of voluntary force generation on the elastic components of endpoint stiffness. Experimental Brain Research. 2001;141(3):312–323. doi:10.1007/s002210100880.

60. Gomi H, Kawato M. Equilibrium-Point Control Hypothesis Examined by Measured Arm Stiffness During Multijoint Movement. Science. 1996;272(5258):117–120. doi:10.1126/science.272.5258.117.

61. Lee H, Krebs HI, Hogan N. Linear time-varying identification of ankle mechanical impedance during human walking. ASME 2012 5th Annual Dynamic Systems and Control Conference Joint with the JSME 2012 11th Motion and Vibration Conference, DSCC 2012-MOVIC 2012. 2012;1:753–758. doi:10.1115/DSCC2012-MOVIC2012-8674.

62. Latash ML. Reconstruction of equilibrium trajectories and joint stiffness patterns during single-joint voluntary movements under different instructions. Biological Cybernetics. 1994;71(5):441–450. doi:10.1007/BF00198920.

63. Domen K, Latash M, Zatsiorsky VM. Reconstruction of equilibrium trajectories during whole-body movements. Biological cybernetics. 1999;80(3):195–204.

64. Hogan N. Physical Interaction via Dynamic Primitives. In: Laumond JP, Mansard N, Lasserre JB, editors. Geometric and Numerical Foundations of Movements. vol. 117 of Springer Tracts in Advanced Robotics. Cham: Springer International Publishing; 2017. p. 269–299. Available from: `http://link.springer.com/10.1007/978-3-319-51547-2_12`.

65. Hermus J, Doeringer J, Sternad D, Hogan N. Separating neural influences from peripheral mechanics: the speed-curvature relation in mechanically constrained actions. Journal of Neurophysiology. 2020;123(5):1870–1885. doi:10.1152/jn.00536.2019.

66. Burdet E, Tee KP, Mareels I, Milner TE, Chew CM, Franklin DW, et al. Stability and motor adaptation in human arm movements. Biological Cybernetics. 2006;94(1):20–32. doi:10.1007/s00422-005-0025-9.

67. Franklin DW, Liaw G, Milner TE, Osu R, Burdet E, Kawato M. Endpoint Stiffness of the Arm Is Directionally Tuned to Instability in the Environment. Journal of Neuroscience. 2007;27(29):7705–7716. doi:10.1523/JNEUROSCI.0968-07.2007.

68. Xiong X, Nah MC, Krotov A, Sternad D. Online Impedance Adaptation Facilitates Manipulating a Whip. In: 2021 IEEE/RSJ International Conference on Intelligent Robots and Systems (IROS). Prague, Czech Republic: IEEE; 2021. p. 9297–9302. Available from: `https://ieeexplore.ieee.org/document/9636663/`.

69. Berret B, Jean F. Stochastic optimal open-loop control as a theory of force and impedance planning via muscle co-contraction. PLOS Computational Biology. 2020;16(2):e1007414. doi:10.1371/journal.pcbi.1007414.

70. Shourijeh MS, Fregly BJ. Muscle synergies modify optimization estimates of joint stiffness during walking. Journal of Biomechanical Engineering. 2020;142(1):1–9. doi:10.1115/1.4044310.

71. Hammoud B, Khadiv M, Righetti L. Impedance Optimization for Uncertain Contact Interactions Through Risk Sensitive Optimal Control. IEEE Robotics and Automation Letters. 2021;6(3):4766–4773. doi:10.1109/LRA.2021.3068951.

72. Rouse EJ, Hargrove LJ, Perreault EJ, Kuiken TA. Estimation of Human Ankle Impedance During the Stance Phase of Walking. IEEE Transactions on Neural Systems and Rehabilitation Engineering. 2014;22(4):870–878. doi:10.1109/TNSRE.2014.2307256.

73. Nayeem R, Bazzi S, Hogan N, Sternad D. Transient Behavior and Predictability in Manipulating Complex Objects. In: 2020 IEEE International Conference on Robotics and Automation (ICRA). IEEE; 2020. p. 10155–10161. Available from: `https://ieeexplore.ieee.org/document/9196977/`.

74. Nayeem R, Bazzi S, Sharif Razavian R, Sadeghi M, Sternad D. Visual information is insufficient to interact with complex dynamic objects. In: 30th Annual Meeting of the Neural Control of Movement. Online; 2021.

75. Krutky MA, Trumbower RD, Perreault EJ. Influence of environmental stability on the regulation of end-point impedance during the maintenance of arm posture. Journal of Neurophysiology. 2013;109(4):1045–1054. doi:10.1152/jn.00135.2012.

76. Mussa-Ivaldi F, Hogan N, Bizzi E. Neural, mechanical, and geometric factors subserving arm posture in humans. The Journal of Neuroscience. 1985;5(10):2732–2743. doi:10.1523/JNEUROSCI.05-10-02732.1985.

77. Dumas R, Chèze L, Verriest JP. Adjustments to McConville et al. and Young et al. body segment inertial parameters. Journal of Biomechanics. 2007;40(3):543–553. doi:10.1016/j.jbiomech.2006.02.013.

78. Meyer DE, Abrams RA, Kornblum S, Wright CE, Keith Smith JE. Optimality in human motor performance: Ideal control of rapid aimed movements. Psychological Review. 1988;95(3):340–370. doi:10.1037/0033-295X.95.3.340.

79. Loram ID, van de Kamp C, Gollee H, Gawthrop PJ. Identification of intermittent control in man and machine. Journal of The Royal Society Interface. 2012;9(74):2070–2084. doi:10.1098/rsif.2012.0142.

80. Joyce GC, Rack PMH, Westbury DR. The mechanical properties of cat soleus muscle during controlled lengthening and shortening movements. The Journal of Physiology. 1969;204(2):461–474. doi:10.1113/jphysiol.1969.sp008924.

81. Rack PMH, Westbury DR. The short range stiffness of active mammalian muscle and its effect on mechanical properties. The Journal of Physiology. 1974;240(2):331–350. doi:10.1113/jphysiol.1974.sp010613.

82. Pando AL, Lee H, Drake WB, Hogan N, Charles SK. Position-Dependent Characterization of Passive Wrist Stiffness. IEEE Transactions on Biomedical Engineering. 2014;61(8):2235–2244. doi:10.1109/TBME.2014.2313532.

83. Georgopoulos AP, Schwartz AB, Kettner RE. Neuronal population coding of movement direction. Science. 1986;233(1986):1416–1419. doi:10.1126/science.3749885.

84. Churchland MM, Cunningham JP, Kaufman MT, Foster JD, Nuyujukian P, Ryu SI, et al. Neural population dynamics during reaching. Nature. 2012;487(7405):51–56. doi:10.1038/nature11129.

85. Shenoy KV, Sahani M, Churchland MM. Cortical Control of Arm Movements: A Dynamical Systems Perspective. Annual Review of Neuroscience. 2013;36(1):337–359. doi:10.1146/annurev-neuro-062111-150509.

86. Russo AA, Khajeh R, Bittner SR, Perkins SM, Cunningham JP, Abbott LF, et al. Neural Trajectories in the Supplementary Motor Area and Motor Cortex Exhibit Distinct Geometries, Compatible with Different Classes of Computation. Neuron. 2020;107(4):745–758. doi:10.1016/j.neuron.2020.05.020.

87. McGeer T. Passive Dynamic Walking. The International Journal of Robotics Research. 1990;9(2):62–82. doi:10.1177/027836499000900206.

88. Collins S, Ruina A, Tedrake R, Wisse M. Efficient Bipedal Robots Based on Passive-Dynamic Walkers. Science. 2005;307(5712):1082–1085. doi:10.1126/science.1107799.

89. Beal DN, Hover FS, Triantafyllou MS, Liao JC, Lauder GV. Passive propulsion in vortex wakes. Journal of Fluid Mechanics. 2006;549(-1):385. doi:10.1017/S0022112005007925.

90. Franceschini N, Pichon JM, Blanes C. From insect vision to robot vision. Philosophical Transactions of the Royal Society of London Series B: Biological Sciences. 1992;337(1281):283–294. doi:10.1098/rstb.1992.0106.

91. Abad SA, Sornkarn N, Nanayakkara T. The role of morphological computation of the goat hoof in slip reduction. In: 2016 IEEE/RSJ International

Conference on Intelligent Robots and Systems (IROS). vol. 2016-Novem. IEEE; 2016. p. 5599–5605. Available from: http://ieeexplore.ieee.org/document/7759823/.

92. Sornkarn N, Dasgupta P, Nanayakkara T. Morphological Computation of Haptic Perception of a Controllable Stiffness Probe. PLOS ONE. 2016;11(6):e0156982. doi:10.1371/journal.pone.0156982.

93. Herzog W. The multiple roles of titin in muscle contraction and force production. Biophysical Reviews. 2018;10(4):1187–1199. doi:10.1007/s12551-017-0395-y.

94. Sternad D, Saltzman EL, Turvey MT. Interlimb coupling in a simple serial behavior: A task dynamic approach. Human Movement Science. 1998;17(3):393–433. doi:10.1016/S0167-9457(98)00006-2.

95. Ronsse R, Sternad D, Lefèvre P. A computational model for rhythmic and discrete movements in uniand bimanual coordination. Neural Computation. 2009;21(5):1335–1370. doi:10.1162/neco.2008.03-08-720.

96. Sternad D, Dean WJ, Schaal S. Interaction of rhythmic and discrete pattern generators in single-joint movements. Human Movement Science. 2000;19(4):627–664. doi:10.1016/S0167-9457(00)00028-2.